JOTCS B
Journal of the Turkish Chemical Society
Section: B
Chemical Engineering
TURKISH CHEMICAL SOCIETY

INVESTIGATION OF ACQUISITION OF TRIPLE SULFURS FROM $Pb(CH_3COO)_2$-Na_3AsO_4-H_2S-H_2O SYSTEM BY HYDROCHEMICAL METHOD

Huseyn Imanov*, Gorkhmaz Huseynov

Institute of Natural Resources of Nakhchivan Branch of Azerbaijan National Academy of Sciences, Nakhchivan city, H. Aliyev street 35, AZ7000, Azerbaijan

Abstract: Acquisition conditions by hydrothermal method of triple sulfides from $Pb(CH_3COO)_2$-Na_3AsO_4-H_2S-H_2O system were investigated using X-ray phase (X-ray), Differential Thermal (DTA) and Scanning Electron Microscopy (SEM) analysis, TG analysis methods. It was determined that sediments were obtained containing $Pb_{26+x}As_{12}S_{44+x}$ content in pH=1-6 range and $Pb_{28-x}As_{12}S_{46-x}$ content (0,6 < x < 1,5) in pH=6-14 range. The durability limits of PbS, As_2S_5, As_2S_3, $Pb(OH)_2$, and Na_3AsO_4 were determined, and pCb-pH (pCb- difference between initial and final concentrations of metal) diagram was formed. The results of the X-ray phase analysis methods indicate that when the precipitates having a Pb:As:S=1:2:4; 2:2:5 and 9:4:15 molar ratio (pH=1-6) are thermally processed in vacuum at 400 °C (~10^{-2} Pa) in a dual-zone regime, phases containing $PbAs_2S_4$, $Pb_2As_2S_5$ and $Pb_9As_4S_{15}$ are conveniently formed. All three compounds are composed of nanoparticles, and high adhesion between particles is observed. Depending on the pH, concentration, and temperature of the condition, a large number of different precipitates and layers are obtained in the $Pb(CH_3COO)_2$-Na_3AsO_4-H_2S-H_2O system. Based on TG analysis, the stoichiometric composition of $PbAs_2S_4$, $Pb_9As_4S_{15}$, and $Pb_2As_2S_5$ compounds was determined.

Keywords: Triple sulfur, hydrochemical sedimentation, semiconductor, concentration, phase, micromorphology.

Submitted: March 02, 2020. **Accepted:** May 26, 2020.

Cite this: Imanov H, Huseynov G. INVESTIGATION OF ACQUISITION OF TRIPLE SULFURS FROM Pb(CH3COO)2-Na3AsO4-H2S-H2O SYSTEM BY HYDROCHEMICAL METHOD. JOTCSB. 2020;3(2):35–40.

***Corresponding author. E-mail:** huseyn.imanov1991@gmail.com.

INTRODUCTION

Thio-salts formed by lead with arsenic are glass semiconductors and are widely used in the radio-electronics industry, such as perspectively materials, or are considered necessary for application. It is known from the literature that there are intermediate phases with the composition $PbAs_2S_4$, $Pb_3As_4S_9$, $Pb_4As_6S_{13}$, $Pb_{13}As_{18}S_{40}$, $Pb_{19}As_{26}S_{58}$, $Pb_2As_2S_5$, $Pb_{27}As_{14}S_{48}$, $Pb_9As_4S_{15}$ etc. in the Pb-As-S system (3). Many of these intermediate phases have been found in minerals found in nature (7, 8). The compounds present in the Pb-As-S system were obtained by vacuum (~900 °C) synthesis, and glasses were prepared by rapidly cooling the alloys. It was found that in the PbS-As_2S_3 system, glasses were obtained in 0-50 mol% PbS concentration areas (3).

Recently, interest in the acquisition of thioarsenides and thioarsenates in different solvent environments has increased (5). There is little information in the literature on the acquisition of thioarsenides and thioarsenates in water and organic solvent conditions. Only (1,2) studies arsenic(V) sulfide was affected with the copper(II) sulfate in aqueous condition, $Cu(AsS_3)_2$ - containing compound (copper(II) metathioarsenate) was obtained and the

effect of the pH and temperature of the condition on its' yield was studied.

With this in mind, we aim to investigate the acquisition condition and properties of thin layers from the $Pb(CH_3COO)_2$-Na_3AsO_4-H_2S-H_2O system.

In this article, the synthesis of some triple sulfides from $Pb(CH_3COO)_2$-Na_3AsO_4-H_2S-H_2O system by X-ray phase, Differential Thermal (DTA) and Scanning Electron Microscopy (SEM), TG analysis methods by the hydrochemical method, micromorphology and depending on conditions (concentration, temperature, and pH of the condition) the results of the composition of phases are given.

EXPERIMENTAL SECTION

Aqueous solutions of $Pb(CH_3COO)_2$ and Na_3AsO_4 were used as primary components to obtain triple sulfides by the hydrochemical method. 0.1 M solutions of the primary substances were mixed at different molar ratios, and H_2S gas was introduced into the solution. Experiments were performed in the range of pH 0-14 to determine the conditions of the formation of the phases. Triple sulfur precipitates were obtained in a chemical cup made of molybdenum glass containing a volume of 100 mL. Sedimentation was completed in 60 minutes at 70 °C. The thermal process of the sediments was carried out under vacuum (~10^{-2} Pa) at 100-400 °C.

Thin layers were obtained to investigate the micromorphology of the phases formed in the $Pb(CH_3COO)_2$-Na_3AsO_4-H_2S-H_2O system. Chemical sedimentation was performed on the glass substrate (Microscope Slides, Cat. No.7101, 25.4x76.2 mm) cleaned with a mixture of $NaHCO_3$, HF, and chrome to obtain thin layers. The substrate was placed in $SnCl_2$ -in hydrochloric acid solution and after 2-3 minutes, washed with boiling distilled water to ensure homogeneous sedimentation on the substrate. Then, 1 M sulfurizing reagent ($(NH_4)_2S$) was added to the solution and left to stand for 2-3 minutes, then washed with hot distilled water. Following these processes, the substrate was placed in a chemical cup, and a reaction mixture was added to it.

Effect of pH of the Solution

The mass of sediments formed at pH=0-14 and the concentration of ions into the solution were determined to determine the acquisition conditions of binary and triple compounds by hydrochemical method from $Pb(CH_3COO)_2$-Na_3AsO_4-H_2S-H_2O system. The durability limits of PbS, As_2S_5, As_2S_3, $Pb(OH)_2$, and Na_3AsO_4 were determined, and pC_b-pH (pC_b- difference between initial and final concentrations of metal) diagram was formed based on the results obtained (Figure 1). The solubility values of the related compounds (PbS, As_2S_5, As_2S_3, $Pb(OH)_2$) mentioned in the literature were used in the calculations (4). 0.5 M HNO_3 and NaOH solutions were used to change the pH of the condition.

Figure 1 shows the common precipitation areas of PbS, As_2S_3, and As_2S_5 in the $Pb(CH_3COO)_2$-Na_3AsO_4-H_2S-H_2O system are observed in the range of pH=0-6. These results have been widely used in the planning of experimental studies.

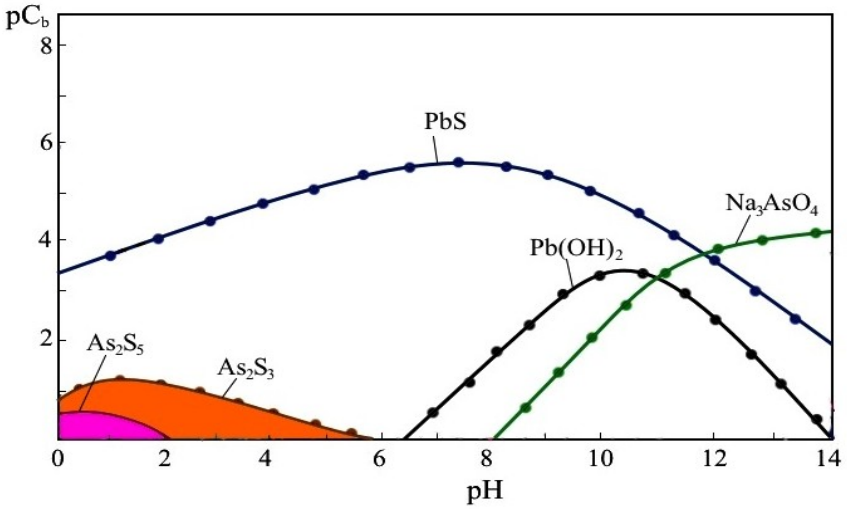

Figure 1: Common deposition areas of PbS, As_2S_3, and As_2S_5 compounds in the $Pb(CH_3COO)_2$-Na_3AsO_4-H_2S-H_2O system: colored areas.

X-ray phase (2D PHASER "Bruker", CuK↙, 2 ⁻ , 10-80 deg.) and chemical analysis methods (gravimetric and volume) revealed that sediments were obtained containing $Pb_{26+x}As_{12}S_{44+x}$ content in pH=1-6 range and $Pb_{28-x}As_{12}S_{46-x}$ content (0.6 < x < 1.5) in pH=6-14 range (Table 1).

Table 1: Composition of sediments obtained from $Pb(CH_3COO)_2$-Na_3AsO_4-H_2S-H_2O system at 70 °C.

The composition of the sediment	pH value
$Pb_{25.6}As_{12}S_{44.9}$	1
$Pb_{25.7}As_{12}S_{44.8}$	2
$Pb_{25.9}As_{12}S_{44.6}$	3
$Pb_{26.2}As_{12}S_{44.6}$	4
$Pb_{26.5}As_{12}S_{44.4}$	5
$Pb_{26.8}As_{12}S_{44.1}$	6
$Pb_{27.2}As_{12}S_{43.3}$	7
$Pb_{27.3}As_{12}S_{42.7}$	8
$Pb_{27.6}As_{12}S_{40.7}$	9
$Pb_{27.8}As_{12}S_{40.2}$	10
$Pb_{27.9}As_{12}S_{40.1}$	11
$Pb_{28.3}As_{12}S_{39.4}$	12
$Pb_{28.5}As_{12}S_{39.0}$	13
$Pb_{28.7}As_{12}S_{34.9}$	14

XRD Analysis

The results of the X-ray phase (2D PHASER "Bruker", CuK_α, 2θ, 10-80 deg.) analysis methods indicate that when the precipitates having a Pb:As:S=1:2:4; 2:2:5 and 9:4:15 molar ratio (pH=1-6) are thermally processed in vacuum at 400 °C (~10^{-2} Pa) in a dual-zone regime, phases containing $PbAs_2S_4$, $Pb_2As_2S_5$ and $Pb_9As_4S_{15}$ are conveniently formed (Figure 2). When the other composition sediments are thermally processed, the mixtures of $PbAs_2S_4$, $Pb_3As_4S_9$, $Pb_4As_6S_{13}$, $Pb_{13}As_{18}S_{40}$, $Pb_{19}As_{26}S_{58}$, $Pb_2As_2S_5$, $Pb_{27}As_{14}S_{48}$, $Pb_9As_4S_{15}$, PbS, As_2S_3 and S phases are obtained. It was determined that the amount of oxygen was range of 7-14.8 mol% in the precipitates obtained in the range of pH = 8-14. It is because the hydrolysis products obtained under the same conditions remain in the precipitates.

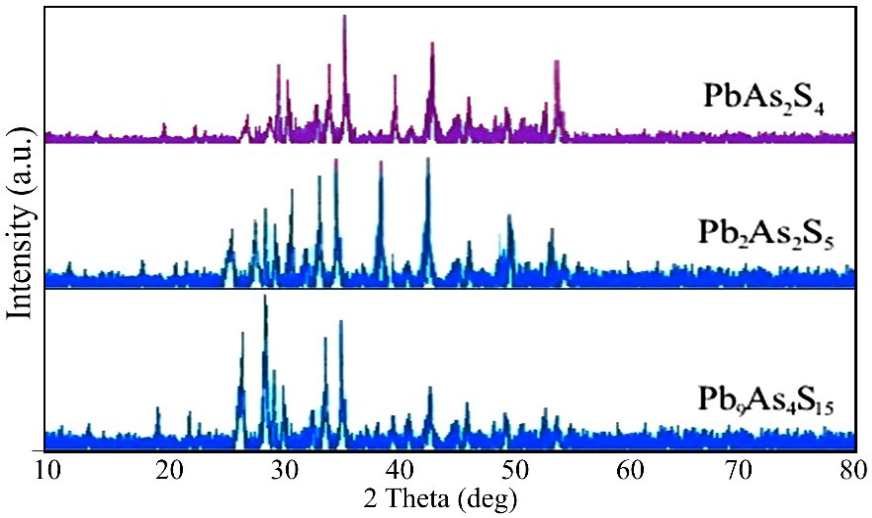

Figure 2: Diffractogram of $PbAs_2S_4$, $Pb_2As_2S_5$ and $Pb_9As_4S_{15}$.

Scanning Electron Microscopy (SEM)

Micromorphology of newly deposited and thermally processed $PbAs_2S_4$, $Pb_2As_2S_5$ and $Pb_9As_4S_{15}$ layers was studied on a HITACHI TM 3000 brand scanning electron microscope (Figure 3).

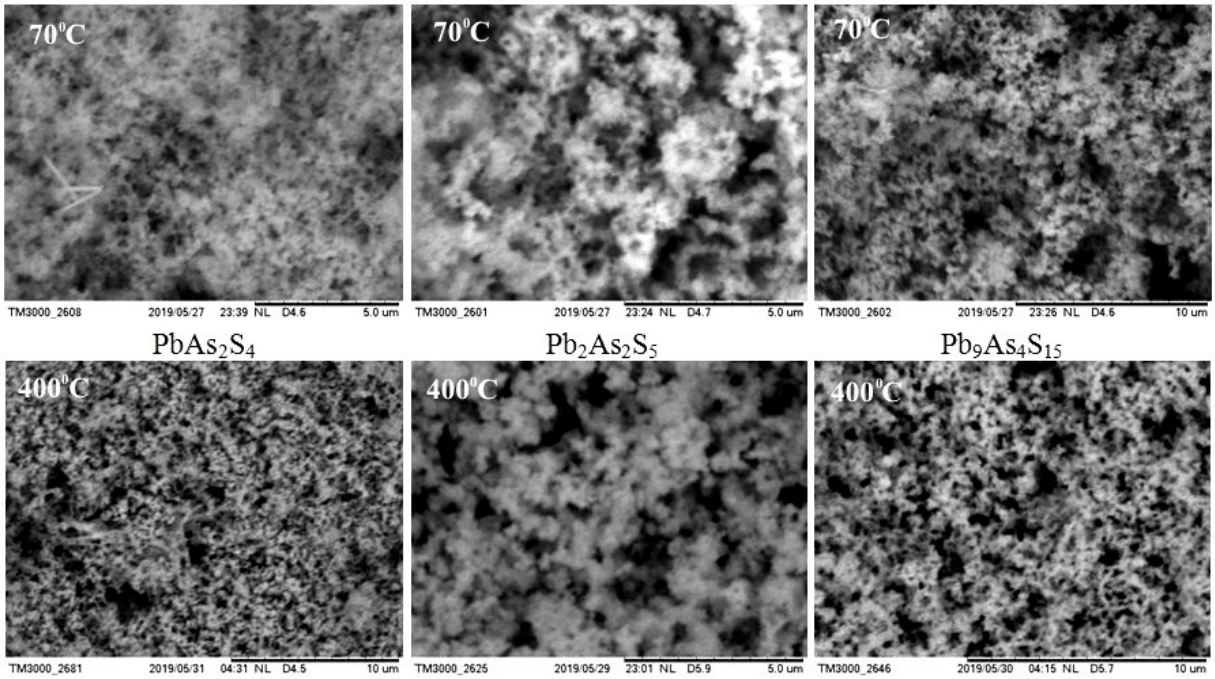

Figure 3: SEM images of $PbAs_2S_4$, $Pb_2As_2S_5$ and $Pb_9As_4S_{15}$ compounds.

As seen from SEM images of the compounds $PbAs_2S_4$, $Pb_2As_2S_5$ and $Pb_9As_4S_{15}$, all three compounds were composed of nanoparticles. High adhesion is observed among the nanoparticles. At 400 °C, the mesh-shaped structure is formed in the thermally processed layers, which increases the size of the particles.

TG analysis

From the DTA (pyrometer HTP-70, device Термоскан -2) results, it is understood that $PbAs_2S_4$ compound melts congruently at 454 °C, $Pb_9As_4S_{15}$ compound is durable to the temperatures of 549 °C, and $Pb_2As_2S_5$ compound melts incongruently at 508 °C. TG analysis (NETZSCH STA 449F3) was performed to determine the stoichiometric composition of $PbAs_2S_4$, $Pb_9As_4S_{15,}$ and $Pb_2As_2S_5$ compounds. Samples were heated under nitrogen-oxygen at 700-800 °C for 1 hour. As seen from the TG curves, the maximum mass loss in $Pb_2As_2S_5$ compound was observed at 340 °C, 690 °C in $PbAs_2S_4$ compound and 660 °C in $Pb_9As_4S_{15}$ compound (Figure 4). The compositions of the compounds were determined based on the maximum mass loss. It has been found that the compounds correspond to formulas $PbAs_2S_4$, $Pb_9As_4S_{15}$ and $Pb_2As_2S_5$ as appropriate.

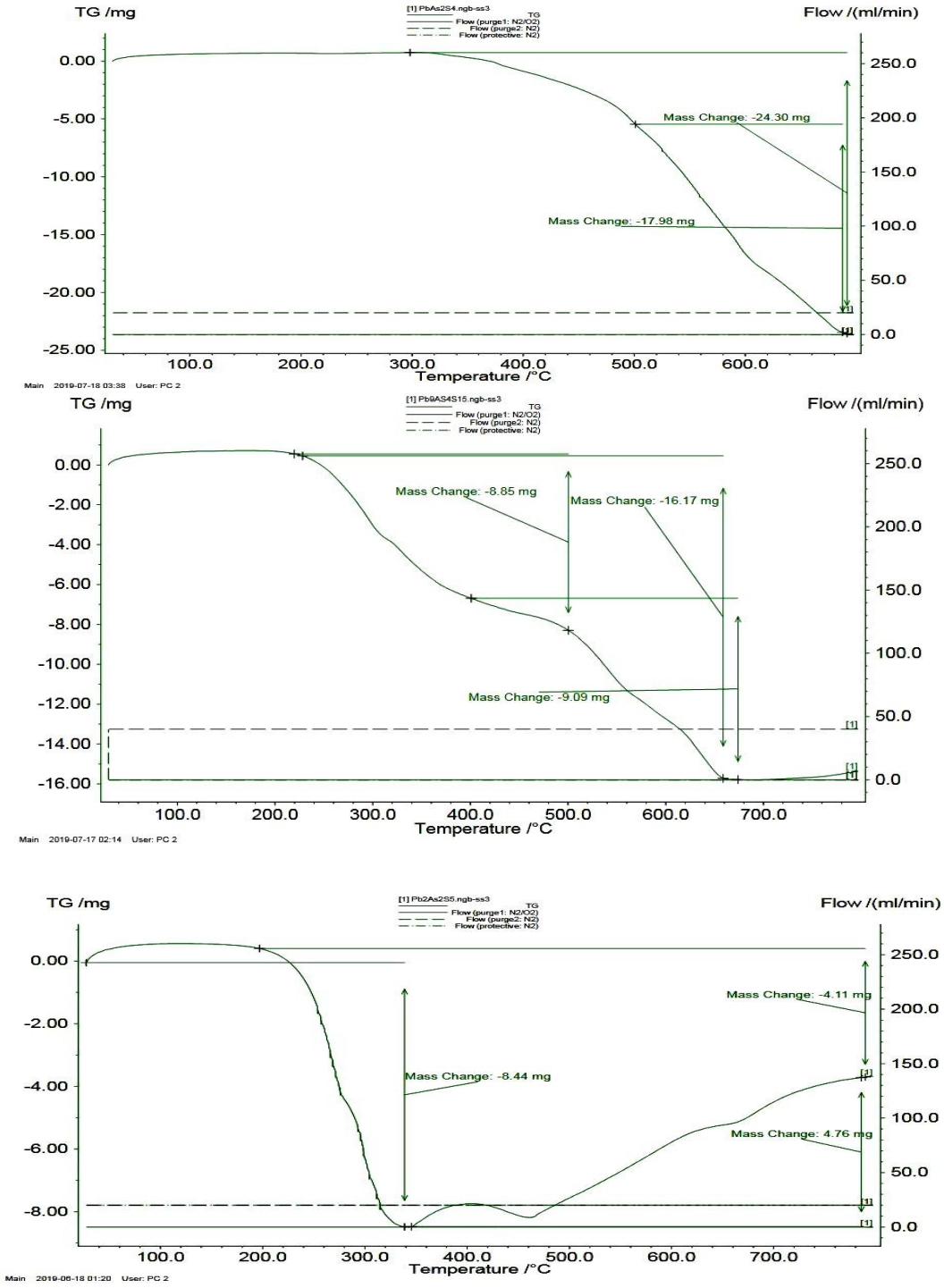

Figure 4: TG curves of $PbAs_2S_4$, $Pb_9As_4S_{15}$ and $Pb_2As_2S_5$.

RESULTS

In general, it is understood from the experimental results that, depending on the conditions, it is possible to obtain a large number of different composition precipitates and layers from the $Pb(CH_3COO)_2$-Na_3AsO_4-H_2S-H_2O system. Arsenic is generally trivalent in the composition of the phases formed when these deposits and layers are thermally processed. It is indicative of the observation that

lead thioarsenates are present only at low temperatures (T < 100 °C). When the temperature rises, they decompose into the corresponding thioarsenites ($PbAs_2S_4$, $Pb_3As_4S_9$, $Pb_4As_6S_{13}$, $Pb_{13}As_{18}S_{40}$, $Pb_{19}As_{26}S_{58}$, $Pb_2As_2S_5$, $Pb_{27}As_{14}S_{48}$, $Pb_9As_4S_{15}$).

CONCLUSIONS

The durability limits of PbS, As_2S_5, As_2S_3, $Pb(OH)_2$ and Na_3AsO_4 were determined by hydrochemical method and pC_b-pH (pC_b- the difference between initial and final concentrations of metal). Depending on the molar ratio of the primary components, it was determined that variable content phases were obtained from $Pb(CH_3COO)_2$-Na_3AsO_4-H_2S-H_2O system at 70 °C. When these phases are thermally processed, mixtures of $PbAs_2S_4$, $Pb_3As_4S_9$, $Pb_4As_6S_{13}$, $Pb_{13}As_{18}S_{40}$, $Pb_{19}As_{26}S_{58}$, $Pb_2As_2S_5$, $Pb_{27}As_{14}S_{48}$, $Pb_9As_4S_{15}$, PbS, As_2S_3 and S phases are formed. The results of the X-ray phase analysis methods indicate that when the precipitates having a Pb:As:S=1:2:4; 2:2:5 and 9:4:15 molar ratio (pH=1-6) are thermally processed in vacuum at 400 °C ($\sim 10^{-2}$ Pa), phases containing $PbAs_2S_4$, $Pb_2As_2S_5$ and $Pb_9As_4S_{15}$ are conveniently formed. All three compounds were composed of nanoparticles and high adhesion is observed among the particles. Based on TG analysis, stoichiometric composition of $PbAs_2S_4$, $Pb_9As_4S_{15}$ and $Pb_2As_2S_5$ compounds were determined.

ACKNOWLEDGMENTS

The study was supported by the Institute of Natural Resources of Nakhchivan Branch of Azerbaijan National Academy of Sciences. The authors are grateful to the organizing committee, head of congress Prof. Dr. Ayfer SARAÇ, Chemical Society of Turkey, Yıldız Technical University for the organizing 31st National Chemistry Congress,with the main theme "starry 100th anniversary of chemistry".

REFERENCES

1. Rzayev B.Z. Arsenin kükürdlü birləşmələri sahəsində yeni tədqiqatlar. Bakı "ELM", 2002, 95 s.

2. Hüseynov Q., İmanov H., Məmmədova S. Natrium-metarsenit və tioasetamid əsasında arsen(V) sulfidin alınması şəraitinin tədqiqi. // NDU "Elmi əsərlər", 2018, s. 184-188.

3. Vinoguradova Gu.Z. Styekloobrazovaniye i fazoviye ravnovyesiya v khalʲkoguyenidnikh sistyemakh. M. : Naooka, 1984. 176 s.

4. Looriye Yo.Yo. Spravochnik po analitichyeskoy khimii. M.: Khimiya, 1989, 448 s.

5. Toolyenin S.S. Guidrokhimichyeskoye osazdyeniye plyenok In_2S_3, In2Se3 i khalʲkopiritnikh strooktoor na ikh osnovye. Diss. k.kh.n., Yekatyerinboorgu, 2015, 197 s.

6. Baghbanzadeh M., Carbone L., Cozzoli P.D., Kappe C.O. Microwave-assisted synthesis of colloidal inorganic nanocrystals. // Angew. Chem. Int. Edit. 50, 2011, P. 11312–11359.

7. Stiven İ. Boldish and William B. White. Optical bahd gaps of selected ternary sulfide minerals. // American Mineralogist, 1998, Vol. 83, P. 865-871.

8. Von B. Ribar und W. Nowacki. Neubestimmung der Kristallstruktur von Gratonit, $Pb_9As_4S_{15}$. // Zeitschrift fur Kristallographie, 1969, Bd. 128, P. 321-338.

JOTCS B
Journal of the Turkish Chemical Society
Section: B
Chemical Engineering
TURKISH CHEMICAL SOCIETY

Removal of Naphthol Blue Black by Heterogeneous Fenton-like Reaction with (Bimetallic Iron-Zinc Nanoparticles)/Carbon Composite Material

Deniz UZUNOĞLU*, **Ege KARADENİZ**, **Ayla ÖZER**
Mersin University, Department of Chemical Engineering, Mersin, Turkey.

Abstract: In this work, the synthesis and characterization of (Fe-Zn NPs)/C were carried out and then it was evaluated as a heterogeneous catalyst in the Fenton-like reaction of Naphthol Blue Black (NBB). The characterization studies showed that the synthesized composite material had an amorphous structure and it contained the elements C, O, Fe, and Zn. In addition, it was observed by SEM analysis that iron-zinc nanoparticles (Fe-Zn NPs) were formed between the carbon microspheres indicating the hydrochar structure. The Fenton-like removal ability of (Fe-Zn NPs)/C was also evaluated and the results demonstrated that (Fe-Zn NPs)/C could be a promising Fenton-like catalyst for the removal of NBB from aqueous solutions. The optimum experimental conditions of this Fenton-like reaction were determined to be as follows: Initial pH was 3.0, H_2O_2 concentration was 50 mM, temperature was 40 °C, and catalyst concentration was 0.25 g/L. The reaction order and rate constant were found as 0.5669 and 4.45, respectively.

Keywords: Composite material, Fenton-like reaction, Heterogeneous catalyst, Hydrochar, Naphthol Blue Black, Wastewater treatment.

Submitted: November 29, 2019. **Accepted:** November 01, 2020.

Cite this: Uzunoğlu D, Karadeniz E, Özer A. Removal of Naphthol Blue Black by Heterogeneous Fenton-like Reaction with (Bimetallic Iron-Zinc Nanoparticles)/Carbon Composite Material. JOTCSB. 41-54;3(2):41-54.

***Corresponding author. E-mail:** denizuzunoglu4@gmail.com.

INTRODUCTION

The rapid urbanization and industrialization have recently caused a serious environmental concern due to the huge amount of wastewater generation. The paper, textiles, dyeing of cloth, printing, pharmaceutical, and cooking industries generate the large quantities of colored wastewater due to the use of dyestuffs (1). The unrestrained discharge of these colored wastewaters into the receiving waters negatively affects the aquatic life and also human life via nutrient cycle because the dyestuffs are mostly toxic, carcinogenic, mutagenic or allergenic (2). Therefore, these types of wastewaters must be treated according to the regulations prior to the discharge of them. There are many physical (coagulation, flocculation, adsorption, ion exchange, membrane filtration, nano filtration, ultra-filtration, reverse osmosis), chemical (advanced oxidation process, electrochemical destruction, ozonation, ultraviolet irradiation), and biological (degradation with algae/enzyme/bacteria, combination of aerobic-anaerobic conditions, adsorption by microbial biomass) methods for the removal of dyestuffs from wastewaters (3). Among them, the advanced oxidation processes (AOP) based on the production of free radicals, such as Fenton, photo-Fenton, sono-Fenton processes, ozonation, electrochemical oxidation, photolysis with H_2O_2, and O_3 electro-Fenton, have great importance for the treatment of the wastewaters containing the dyestuffs, which are difficult to remove by conventional methods. In the Fenton processes, highly oxidizing •OH radicals are used to oxidize the dyestuffs. It provides the degradation of complex structured dyestuffs to smaller organic molecules or the completely oxidization of it to CO_2 and H_2O (4). Homogeneous Fenton process, in which soluble iron acts as the catalyst, has been extensively studied and widely applied commercially for the dyestuff treatment (5). However, the difficulty of the homogenous catalyst recovery and tight pH range for reaction are reported as disadvantages (6). In order to overcome these disadvantages of the homogeneous Fenton process, some attempts have been made to develop heterogeneous catalysts, especially iron based

nanoparticles. The metallic and bimetallic iron nanoparticles can be synthesized by various methods such as chemical precipitation, microemulsion, hydrothermal synthesis, thermal degradation, sonochemical synthesis, and electrochemical deposition (7). The most common disadvantages of the metallic nanoparticles is the leaching of metal ions to the medium and the aggregation of them, resulting in a low catalytic activity (8,9). In order to improve the catalyst activity (to prevent the leaching and the aggregation) of the nanoparticles synthesized by these methods, the nanoparticles can be combined with various carbonaceous materials such as cellulose, glucose, agricultural waste, animal manure, food waste, and so on (10). Hydrochar, which is a solid product from a carbonization process of these biomasses, has attracted much attention due to its unique properties. Several thermochemical methods such as combustion, aerial gasification, pyrolysis, and hydrothermal carbonization could be applied for the carbonization process. Among them, the hydrothermal carbonization method have the advantages of being more economical and easy applicability. The hydrothermal carbonization could be carried out at mild conditions (180-250 °C and 20-40 bar) and it does not require pre-drying unlike other methods (11). In the literature, hydrochar has been widely used for supporting various nanoparticles and these hydrochar supported-nanoparticles could be effectively used in the catalytic wastewater treatment processes. For instance, Liang et al. (2017) have investigated the heterogeneous photo-Fenton degradation of organic pollutants with amorphous Fe-Zn-oxide/hydrochar under visible light irradiation (12); Ma et al. (2018) have evaluated the iron nanoparticles in situ encapsulated in lignin-derived hydrochar as an effective catalyst for phenol removal(8); Khataee et al. (2017) have studied on the ultrasound-assisted removal of Acid Red 17 using nanosized Fe_3O_4-loaded coffee waste hydrochar (15); Liu et al. (2016) have reported that nanoscale zerovalent iron loaded on porous carbon showed high performance for removal of carcinogenic polychlorinated biphenyls from aqueous solutions (16); Gai et al. (2017) used the iron nanoparticles immobilized into the porous hydrochar for catalytic decomposition of phenol (17). In this respect, (bimetallic iron-zinc nanoparticles)/carbon composite material [(Fe-Zn NPs)/C] was synthesized by combined co-precipitation/hydrothermal carbonization method and then, [(Fe-ZnNPs)/C] was evaluated as a heterogeneous catalyst in the Fenton-like reaction of Naphthol Blue Black (NBB) dyestuff.

EXPERIMENTAL SECTION

Materials

$Fe(NO_3)_3.9H_2O$ (Acros), $ZnCl_2$ (Merck), D-glucose (Alfa-Aesar), NaOH (Merck), HCl (Sigma-Aldrich), H_2O_2 (Merck), NBB (Merck) are of analytical grade and they were used without any purification.

Synthesis and Characterization of (Bimetallic Iron-Zinc Nanoparticles)/Carbon Composite Material

In the synthesis of (bimetallic iron-zinc nanoparticles)/carbon composite material [(Fe-Zn NPs)/C]; $Fe(NO_3)_3$, $Zn(NO_3)_2$, and D-glucose were dissolved in 60 mL of distilled water and then, the solution pH was adjusted to 11 with the NaOH solution and it was magnetically stirred for 1.0 h. After that, the obtained black-colored suspension containing bimetallic Fe-Zn NPs was autoclaved at 130 °C for 10 h in a Teflon-lined stainless steel autoclave. After the autoclave process, [(Fe-ZnNPs)/C] was obtained and then, it was washed several times with distilled water and dried at 110 ºC for 6 h. [(Fe-ZnNPs)/C] was stored in the refrigerator at +4 °C for further experiments (12). The characterization of [(Fe-ZnNPs)/C] was performed using Scanning Electron Microscope (SEM-Zeiss/ Supra 55, Germany), Energy Dispersive X-ray Spectroscopy (EDX- Zeiss/Supra 55, Germany), and Powder X-ray Diffractometer (XRD-Philips XPert, Netherlands).

Removal of Naphthol Blue Black via Fenton-like Reaction

In the Fenton-like experiments, the desired amount of (Fe-Zn NPs)/C was added to 100 mL of NBB dyestuff solutions at desired initial pH and initial dye concentrations. The flasks containing the solutions were agitated in the water bath for 30 minutes to make certain desorption-adsorption equilibrium of NBB dyestuff aqueous solution with the catalyst. Then, 5 mL of H_2O_2 solution were added to the aqueous dyestuff solutions including the catalyst. After that, the samples were taken at pre-determined time intervals and the catalyst were removed by centrifugation. The concentration of NBB dyestuff was observed by using the UV-Vis spectrophotometer at 628 nm wavelength. The decolorization percentage for NBB dyestuff was expressed in terms of the decrease in UV-Vis absorbance. All of experiments were performed in triplicate and the results were presented as the mean of these experiments.

RESULTS AND DISCUSSIONS

Characterization of (Fe-Zn NPs)/C

The structure and phase purity of (Fe-Zn NPs)/C were investigated by XRD analysis. The obtained XRD pattern of (Fe-Zn NPs)/C was given in Figure 1. Accordingly, narrow and sharp peaks showing a certain crystal structure could not be obtained; however, only a wide peak was obtained at 20º, which is related to the amorphous and non-graphite carbon structure (12-14). As a result, the composite material synthesized in this study does not have a specific crystalline structure; it is an amorphous

material.

The elemental content of (Fe-Zn NPs)/C was determined by EDX analysis. The corresponding SEM image of (Fe-Zn NPs)/C and EDX mapping images were shown in Figures 2 (a)-(f). Accordingly, the microspheres had the element of carbon indicating the structure of a hydrochar while the iron-zinc nanoparticles (Fe-Zn NPs) formed between the microspheres had the elements of iron, zinc, and oxygen. Besides, (Fe-Zn NPs)/C contained 58 %, 12 %, 19 %, and 10% by mass of carbon, oxygen, iron, and zinc elements, respectively.

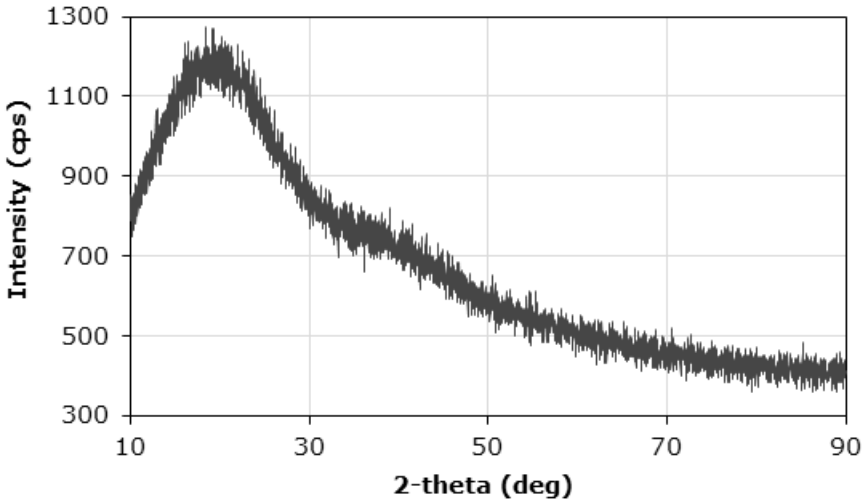

Figure 1. XRD pattern of (Fe-Zn NPs)/C.

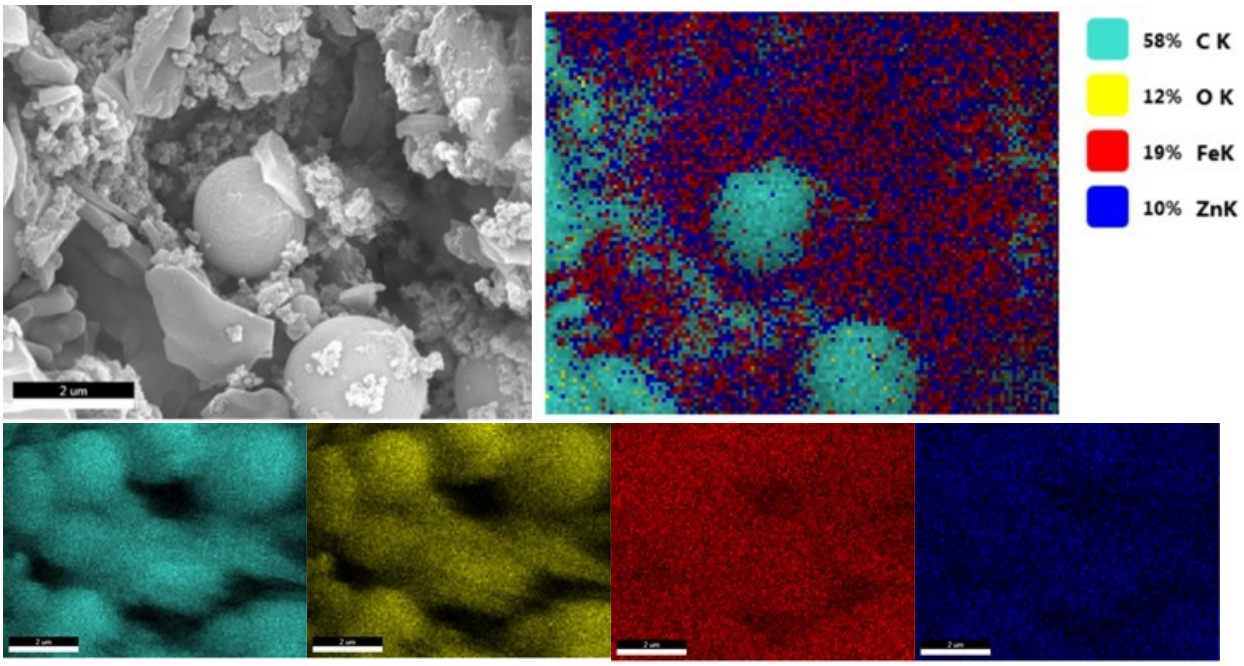

Figure 2. (a) The corresponding SEM image of (Fe-Zn NPs)/C, **(b)** EDX mapping image of (Fe-Zn NPs)/C, **(c)** Carbon mapping, **(d)** Oxygen mapping, **(e)** Iron mapping, **(f)** Zinc mapping.

In this study, (Fe-Zn NPs)/C as well as [(Fe NPs)/C] and [(Zn NPs)/C] were synthesized and their morphologies were investigated by SEM analysis given in Figure 3 (a)-(j). According to Figure 3(a) and (b), it was observed that the (Fe-Zn NPs) formed between the carbon microspheres indicating the hydrochar structure as observed in EDX analysis. The blown-up images of the nanoparticles between the microspheres was presented in Figure 3(c) and (d). SEM images of (Fe-Zn NPs)/C after the Fenton-like reaction were given in Figures 3(e) and (f). The mean particle size of the nanoparticles before the Fenton-like reaction was calculated as 37.43±2.77 nm by Image-J program whilst this value was calculated as 68.84±8.79 nm after the removal of NBB dyestuff via Fenton-like reaction. This particle size analysis via Image-J program was performed with at least 100 particles. As a result,

mostly regular spherical nanoparticles were observed before the Fenton-like reaction while after the Fenton-like reaction, both the particle size increased due to the agglomeration of the nanoparticles, and the regular spherical forms of the nanoparticles destroyed. It could be clearly seen in Figure 3(g) and (i) that the nanoparticles (Fe NPs or Zn NPs) formed between the carbon microspheres. The blown-up images of the nanoparticles in Figure 3(h) and (j) showed that Fe NPs were in spherical forms while Zn NPs were in lamellar forms.

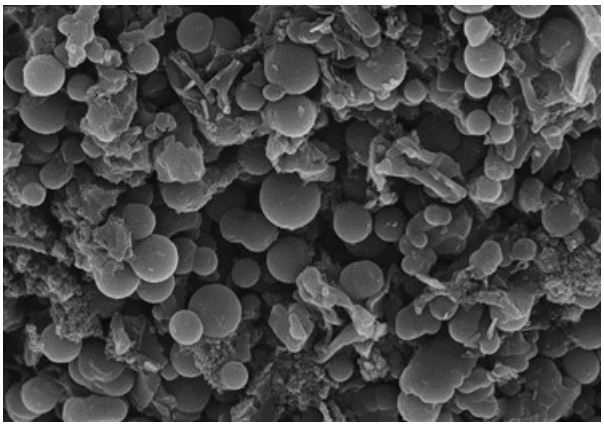

(a)

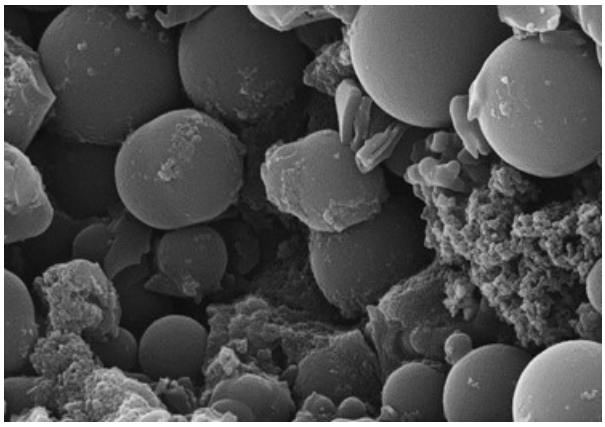

(b)

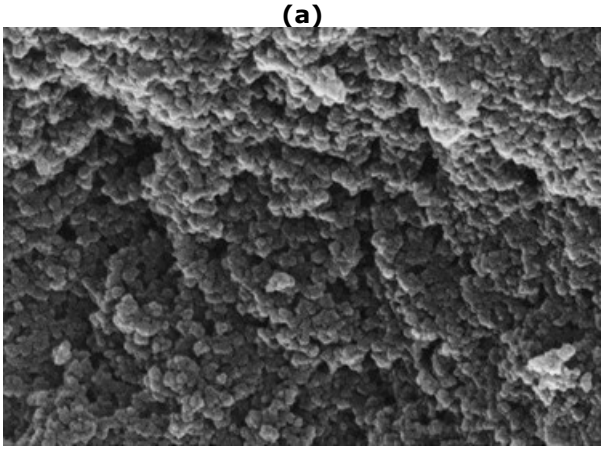

(c)

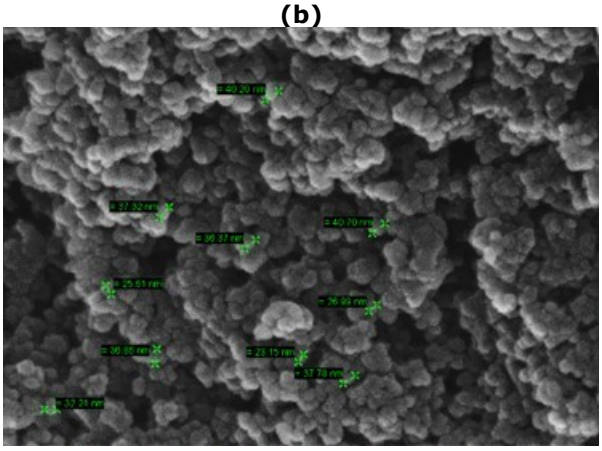

(d)

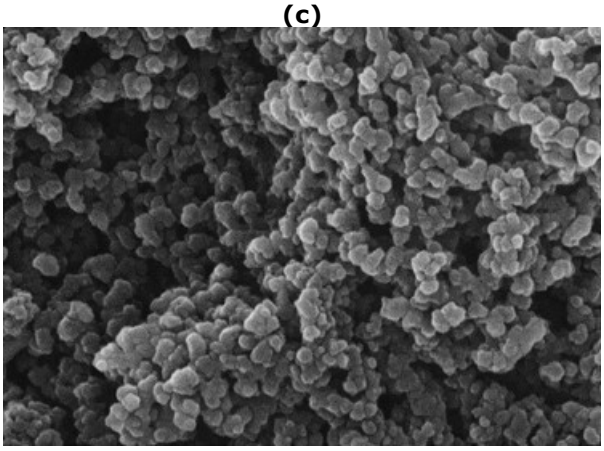

(e)

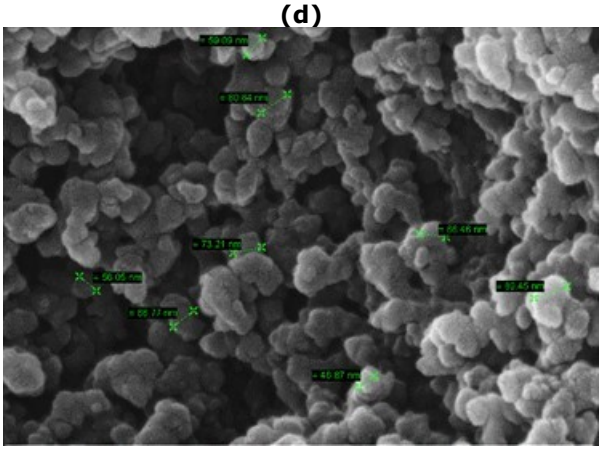

(f)

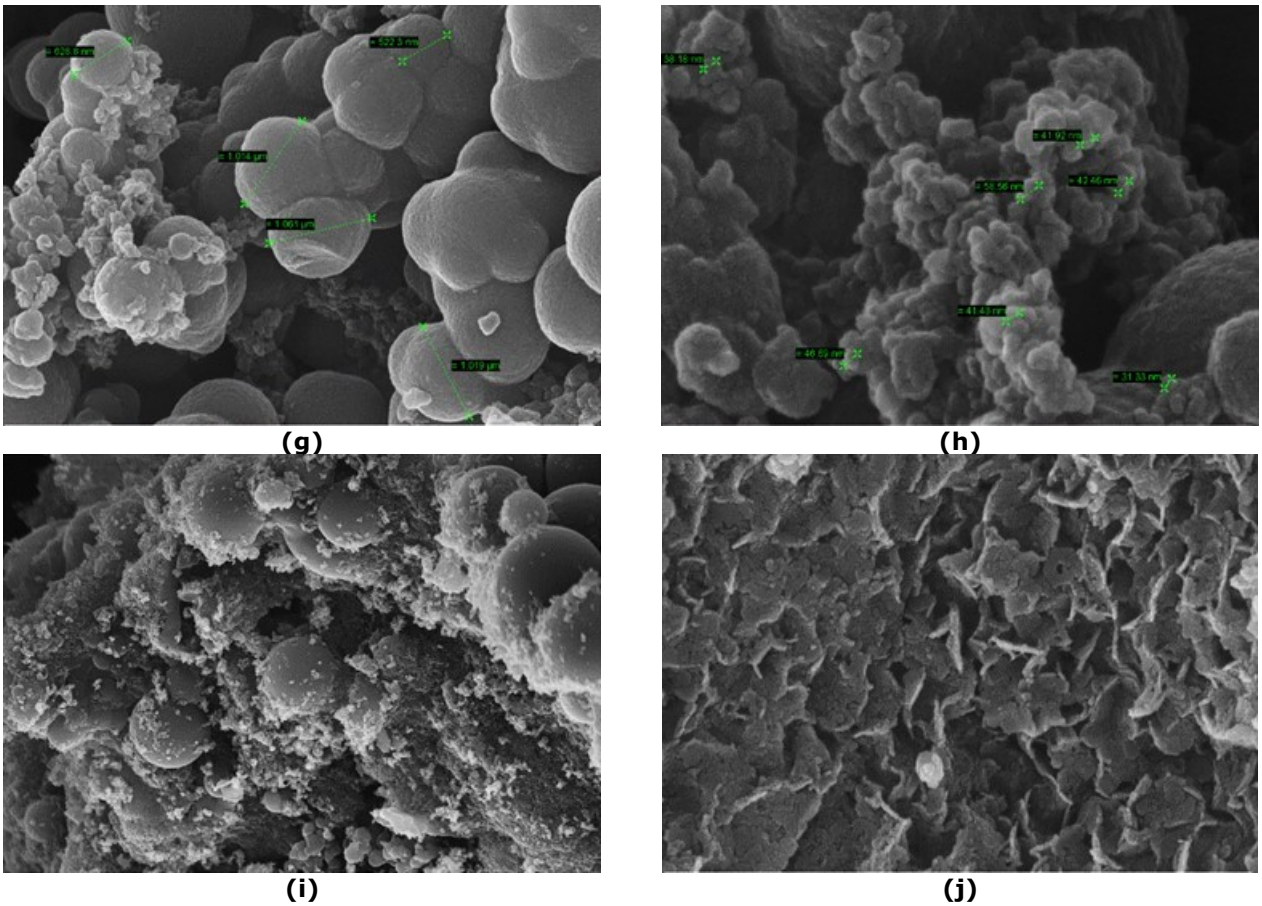

Figure 3.SEM images of **(a)** (Fe-Zn NPs)/C at 10.00 KX before the reaction, **(b)**(Fe-Zn NPs)/C at 30.00 KX before the reaction, **(c)**(Fe-Zn NPs)/C at 100.00 KX before the reaction, **(d)**(Fe-Zn NPs)/C at 200.00 KX before the reaction, **(e)**(Fe-Zn NPs)/C at 100.00 KX after the reaction, **(f)**(Fe-Zn NPs)/C at 200.00 KX after the reaction, **(g)** [(Fe NPs)/C] at 50.00 KX before the reaction, **(h)** [(Fe NPs)/C] at 200.00 KX before the reaction, **(i)** [(Zn NPs)/C] at 10.00 KX before the reaction, **(j)** [(Zn NPs)/C] at 100.00 KX before the reaction.

The specific surface area of (Fe-Zn NPs)/C was observed by using the following equation:

$$S = \frac{q \times N \times A}{M} \quad \text{(Eq. 1)}$$

where S is the specific surface area (m^2/g (Fe-Zn NPs)/C), q is the maximum adsorption capacity of (Fe-Zn NPs)/C at the specific experimental conditions (g dye/g (Fe-Zn NPs)/C), N is the Avogadro's number (6.02×10^{23}); A is the cross-sectional area of methylene blue dye (m^2), and M is the molecular weight of methylene blue (18). In order to calculate the specific surface area, the methylene blue (MB) adsorption experiment with (Fe-Zn NPs)/C was carried out at 40 ºC, 100 mg/L initial dye concentration, natural pH (9.0), 1.0 g/L adsorbent concentration, and 480 min contact time. At these experimental conditions, the maximum adsorption capacity of (Fe-Zn NPs)/C for MB was determined to be 38.21 mg/g. The molecular weight and cross-sectional area of MB dye are 319 g/mole and 1.2×10^{-18} m^2 in a close-packed monolayer, respectively. By using these values, the specific surface area was calculated from Eq. (1) as 86.53 m^2/g (Fe-Zn NPs)/C.

A literature survey was performed for the comparison of specific surface area of nanoparticles-based hydrochar materials and the results were summarized in Table 1. Accordingly, except for the porous hydrochar materials, the specific surface area of (Fe-Zn NPs)/C synthesized in this study had relatively higher than the others. Therefore, it can be concluded that (Fe-Zn NPs)/C synthesized in this study could be evaluated as effective catalyst for the removal of NBB.

Table 1. Comparison of specific surface area of nanoparticles-based hydrochar materials

Material	Specific surface area (m^2/g)	Reference
Fe_3O_4-loaded coffee waste hydrochar	34.7	(19)
Fe-modified hydrochar from orange peel	72.5	(20)
Fe-Zn-oxide/hydrochar	76.8	(12)
(Fe-Zn NPs)/C	86.5	**This work**
Hydrochar functionalized Fe–Mn binary oxide nanocomposites	167.17	(21)
Zerovalent iron nanoparticles supported on hydrochar-derived porous carbon	423	(22)
Hydrochar-supported bimetallic Ni−Cu nanocatalysts	431.8	(23)
Iron nanoparticles immobilized into the porous hydrochar	446	(24)

Removal of NBB Dyestuff with Heterogeneous Fenton-like Reaction

Determination of Heterogeneous Fenton-like Catalyst Properties of (Fe-Zn NPs)/C and Its Compounds

The heterogeneous Fenton-like catalyst properties of (Fe-Zn NPs)/C and its compounds such as Fe-Zn NPs, Fe NPs/C, and Zn NPs/C were determined by calculating removal efficiencies of them for the selected model pollutant of NBB dyestuff removal. Accordingly, the color removal capacities of (Fe-Zn NPs)/C, [(FeNPs)/C], Fe-Zn NPs, and [(Zn NPs)/C] were 96.61, 68.08, 48.43, and 26.01 mg/g, respectively (experimental conditions: initial pH 3.0, 100 mg/L initial dyestuff concentration, 50 mM H_2O_2 concentration, 1.0 g/L catalyst concentration, 25 °C temperature). As a result, the Fenton-like removal studies for NBB dyestuff were performed with (Fe-Zn NPs)/C because it had the maximum color removal capacity among the other catalysts.

Effect of Environmental Conditions of Fenton-like Removal of NBB Dyestuff with (Fe-Zn NPs)/C

The initial pH of solution is a substantial parameter to design a treatment process. For this reason, the effect of initial pH on the removal of NBB dyestuff with (Fe-Zn NPs)/C was investigated at the experimental conditions of 100 mg/L initial dyestuff concentration, 50 mM H_2O_2 concentration, 1.0 g/L catalyst concentration, 25 °C temperature for the initial pH range of 3.0-5.0. The color removal capacities at the equilibrium time of 90 min in the initial pH range of 3.0-5.0 were shown in Figure 4. The color removal capacities at the equilibrium time of 90 min for initial pH 3.0, 5.0, 7.0, and 8.0 were determined to be 96.40±0.36, 95.59±0.61, 94.13±0.25, and 90.19±0.44 mg/g, respectively. Accordingly, the color removal capacities decreased slightly with the increase in the initial pH. Therefore, it could be suggested that this process enables studying at wide initial pH range, which is an advantage for industrial applications. The increase of initial pH causes the decomposition of H_2O_2 to O_2 and H_2O; and so, fewer OH• radicals are formed during the reaction; as a result, the removal percentages reduce with the increase in the initial pH. Another reason may be the decrease in oxidation potentials of the produced OH• radicals at the higher initial pH values; and therefore, the removal percentages may be reduced with the increase in the initial pH (15). For these reasons, the studying at mild acidic conditions can be suggested for the removal of NBB dyestuff with (Fe-Zn Nps)/C.

The effect of H_2O_2 concentration on the removal of NBB dyestuff was investigated by varying H_2O_2 concentration from 1.0 mM to 50 mM at the other fixed conditions (initial pH, 3.0, initial dyestuff concentration, 100 mg/L, catalyst concentration, 1.0 g/L, temperature, 25 °C). The color removal capacities at the equilibrium time of 90 min in the H_2O_2 concentration range of 1.0-50 mM were shown in Figure 5. The color removal capacities at the equilibrium time of 90 min for H_2O_2 concentration of 1.0, 5.0, 10, 15, 25, and 50 mM were observed as 20.03±0.82, 55.51±0.41, 73.55±0.37, 85.57±0.42, 93.42±0.42, and 96.40±0.36 mg/g, respectively. As can be seen in Figure 5, the color removal capacities increased prominently with an increase in H_2O_2 concentration from 1.0 mM to 15 mM, and the increase rate thereafter declined. The reason for this slowdown in the increase rate at the higher H_2O_2 concentrations may be explained with the scavenging effect of OH• radical. At higher H_2O_2 concentrations, the formed OH• radicals reacted with H_2O_2 in the medium and the less oxidative radicals of HO_2• formed at the end of the reaction (H_2O_2 + OH• → HO_2• + H_2O), and so, the color removal amounts decreased at the higher H_2O_2 concentrations because there were fewer strong radicals of OH• in the medium (15). Consequently, because the maximum color removal capacity was obtained at 50 mM H_2O_2 concentration, the other experiments were carried out by using 50 mM H_2O_2.

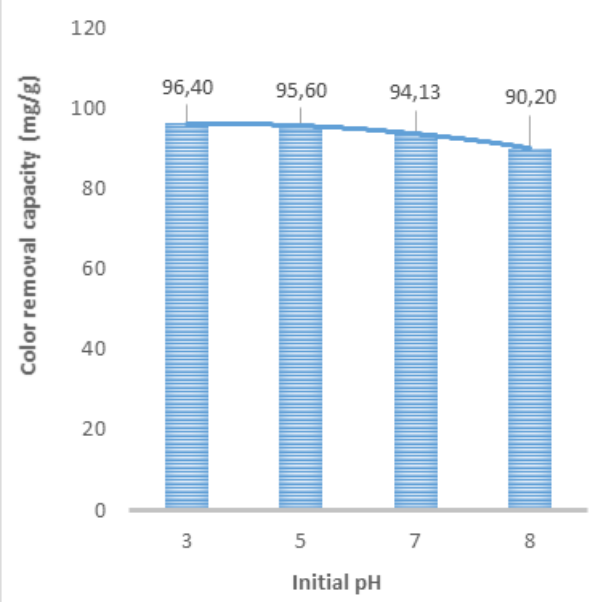

Figure 4. The effect of initial pH (experimental conditions: initial dyestuff concentration, 100 mg/L, H_2O_2 concentration, 50 mM, catalyst concentration, 1.0 g/L, temperature, 25°C)

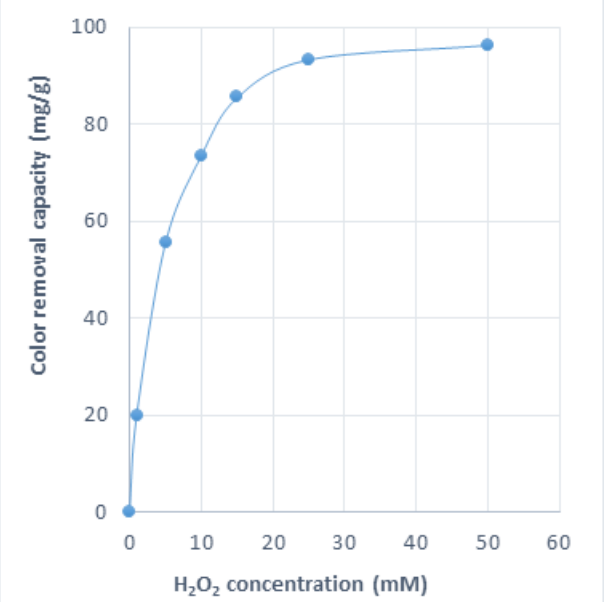

Figure 5. The effect of H_2O_2 concentration (experimental conditions: initial pH 3.0, 100 mg/L initial dyestuff concentration, 1.0 g/L catalyst concentration, 25°C temperature)

The effect of temperature on the removal of NBB dyestuff with (Fe-Zn NPs)/C was investigated at the experimental conditions of initial pH of 3.0, initial dyestuff concentration, 100 mg/L, H_2O_2 concentration, 50 mM, catalyst concentration, 1.0 g/L for the temperature range of 25-55 ºC. The color removal capacities in the temperature range of 25-55 ºC were presented in Figure 6. The color removal capacities at the equilibrium time of 90 min for temperature of 25, 30, 40, 50, and 55 ºC were obtained to be 96.40±0.36, 98.68±0.49, 102.35±0.23, 97.98±0.43, and 85.55±0.45 mg/g, respectively. As shown in Figure 6, the color removal capacity increased up to 40 ºC, and then it decreased slightly. Accordingly, this process enables to study at the wide temperature range, which is an advantage for the industrial applications. On the other hand, the optimum temperature could be selected as 40 ºC due to the obtained maximum color removal capacity at this temperature.

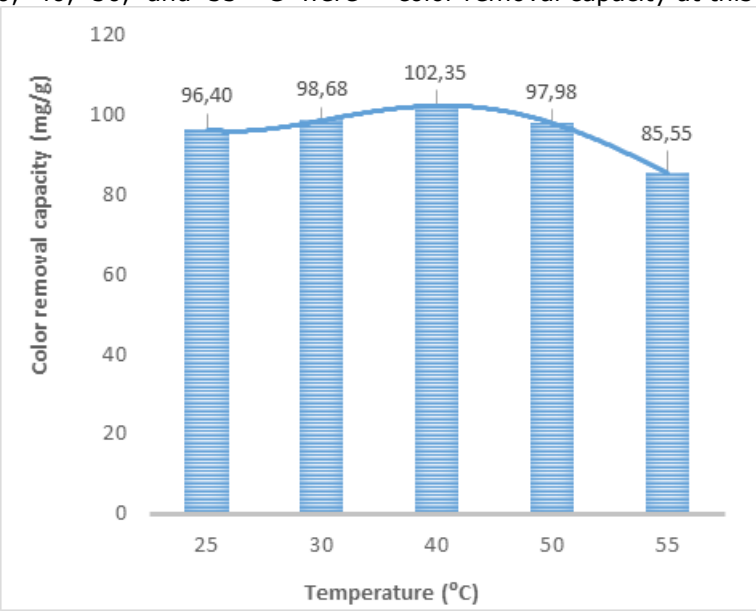

Figure 6. The effect of temperature (experimental conditions: initial pH, 3.0, initial dyestuff concentration, 100 mg/L, H_2O_2 concentration, 50 mM, catalyst concentration, 1.0 g/L).

The effect of initial dyestuff concentration on the removal of NBB dyestuff was investigated by varying initial dyestuff concentration from 100 mg/L to 1200 mg/L at the other fixed conditions (initial pH, 3.0, H_2O_2 concentration, 50 mM, catalyst concentration, 1.0 g/L, temperature, 40 °C). The color removal

capacities at the equilibrium time of 90 min in the initial dyestuff concentration range of 100-1200 mg/L were shown in Figure 7. The color removal capacities at the equilibrium time of 90 min for initial dye concentration of 100, 200, 300, 500, 700, 1000, and 1200 mg/L were determined as 102.35±0.23, 193.51±0.41, 266.53±0.45, 431.69±0.35, 524.59±0.30, 524.66±0.46, and 525.54±0.41 mg/g, respectively. As can be seen in Figure 7, the color removal capacity increased up to 700 mg/L, and it remained nearly constant thereafter. This could be explained as follows (25):

(a) The increase in the initial dyestuff concentration causes adsorption of dyestuff molecules on the surface of catalyst, and so, dyestuff molecules adsorbed on the surface of catalyst may block the active sites of catalyst. As a result, fewer •OH radicals are formed and thus, the color removal capacities may decline.

(b) When there are more dyestuff molecules in the reaction medium, they compete against the intermediates produced during the Fenton-like reaction and thus, the color removal capacities may decline.

The effect of contact time on the removal of NBB dyestuff was investigated by varying initial dyestuff concentration from 100 mg/L to 1200 mg/L at the other fixed conditions (initial pH, 3.0, H_2O_2 concentration, 50 mM, catalyst concentration, 1.0 g/L, temperature, 40 °C). The changes of color removal capacities with contact time for the different initial dyestuff concentrations were shown in Figure 8. As can be seen in Figure 8, the removal capacities increased by increasing contact time up to 90 min and then remained constant indicating that a maximum removal was attained. Therefore, the equilibrium time for the removal of NBB dyestuff with (Fe-Zn NPs)/C was determined to be 90 min.

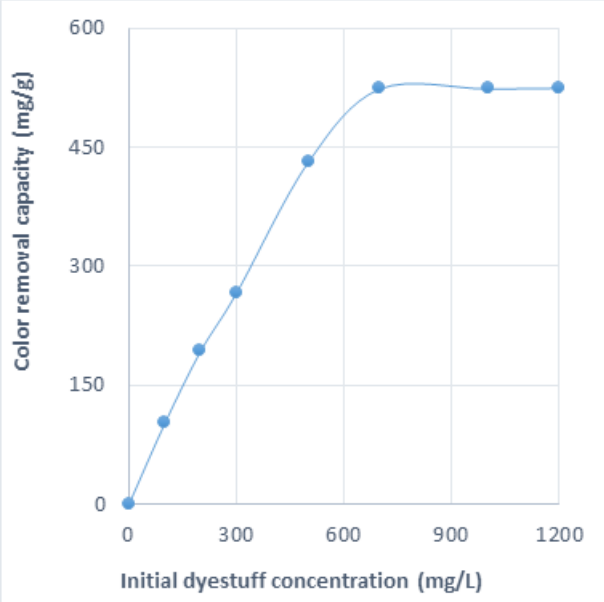

Figure 7. The effect of initial dyestuff concentration (experimental conditions: initial pH, 3.0, H_2O_2 concentration, 50 mM, catalyst concentration, 1.0 g/L, 40 °C temperature)

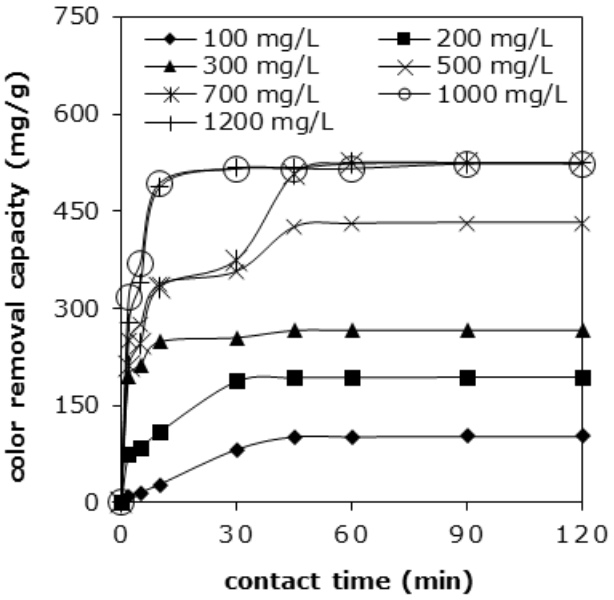

Figure 8. The effect of contact time (experimental conditions: initial pH, 3.0, H_2O_2 concentration, 50 mM, catalyst concentration, 1.0 g/L, 40 °C temperature)

The effect of catalyst concentration on the removal of NBB dyestuff with (Fe-Zn NPs)/C was investigated at the experimental conditions (initial pH, 3.0, initial dyestuff concentration, 100 mg/L, H_2O_2 concentration, 50 mM, temperature, 40 °C for the catalyst concentration range of 0.25-3.0. The color removal capacities at the equilibrium time of 90 min in the catalyst concentration range of 0.25-3.0 were shown in Figure 9. The color removal capacities at the equilibrium time of 90 min for catalyst concentration of 0.25, 0.50, 1.0, 2.0, and 3.0 g/L were obtained as 472.84±0.42, 216.98±0.39, 102.35±0.23, 75.71±0.51, and 72.39±0.49 mg/g, respectively. As seen in the figure, color removal capacities decreased with increasing catalyst concentration. In general, color removal capacity is expected to increase with the increase in the catalyst concentration because the more catalysts are present in the reaction medium, the more H_2O_2 is expected to decompose to OH• radicals. However, it has been reported in the literature that the excessive catalyst loading causes a decrease in the color removal due to the scavenging effect of OH• radicals. Accordingly, the formed OH• radicals react with the excess iron ions in the reaction medium, arising from the iron based catalyst, (Fe^{2+} + OH• → Fe^{3+} + OH^-) (26). For the same reason, the catalyst concentrations higher than 0.25 g/L caused the reduction of the color removal capacities in this study, the optimum catalyst concentration was

therefore determined as 0.25 g/L.

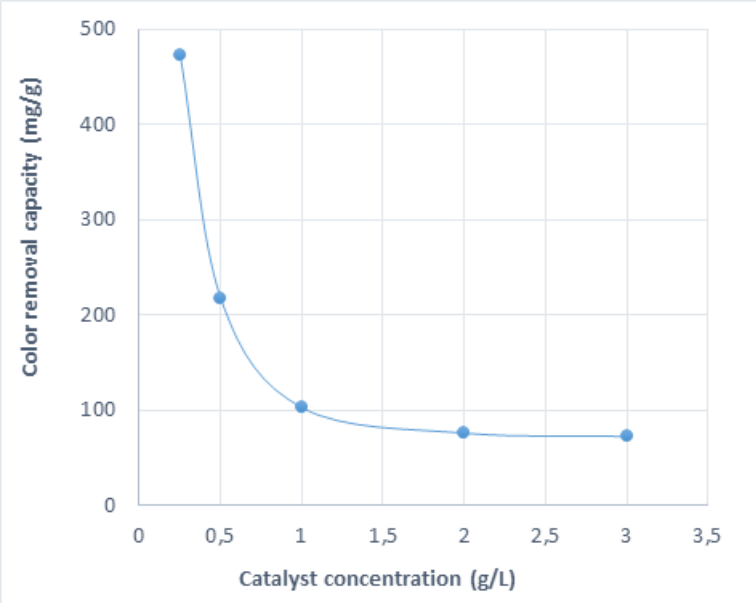

Figure 9. Effect of catalyst concentration (experimental conditions: initial pH, 3.0, initial dyestuff concentration, 100 mg/L, H_2O_2 concentration, 50 mM, temperature, 40°C).

The optimum experimental conditions of this Fenton-like reaction were determined as follows: initial pH, 3.0, H_2O_2 concentration, 50 mM, temperature, 40 °C, and catalyst concentration, 0.25 g/L. At these conditions for initial dye concentration of 100 mg/L, color removal and COD removal percentages were obtained as 100% and 37.6±3.75%, respectively. Although the color removal percentage of 100% showed that the chromophore group of NBB was completely destroyed, the COD removal percentage of 37.6±3.75% indicated the partially oxidation of the dye molecules to CO_2 and H_2O.

A literature survey was performed for the comparison of color removal methods for NBB removal and the results were summarized in Table 2. Accordingly, NBB removal with heterogeneous Fenton-like reaction was firstly evaluated in the literature with this study and in this study, the color removal that could be competitive with other removal methods has been achieved at mild conditions. Moreover, it is an important advantage of this study that 100% color removal can be achieved at the higher initial dye than the most of the studies given in Table 2, which could provide treating the wastewaters containing high dye concentrations.

Table 2. Comparison of color removal methods for NBB removal.

Method of color removal	Experimental conditions	Percentage of color removal (%)	Reference
Fenton-like reaction	Initial dye concentration: **100 mg/L**, pH: 3.0, H_2O_2 concentration: 50 mM, temperature: 40 ºC, catalyst concentration: 0.25 g/L	100	**This work**
Microwave assisted adsorption	Microwave power: 20 W, pH: 3, initial dye concentration: **2.5 mg/L**, catalyst amount: 50 mg	100	(27)
Sonolytic degradation	Initial dye concentration: **5 mg/L**, persulfate concentration: 500 mg/L, frequency: 1700 kHz, temperature: 25 ºC, pH: 6.0	100	(28)
Sonolytic degradation	Initial dye concentration: **5 mg/L**, temperature: 25 ºC, natural pH, frequency: 585 kHz	100	(29)
Photo-catalytic degradation	PH: 3, initial dye concentration: **15 mg/L**, catalyst concentration: 1 g/L	99.74	(30)
Sono-photo-catalytic degradation	Initial pH: 11.0, H_2O_2 concentration: 44.1 mmol/L, Fe-TiO_2 catalyst concentration: 2.2 g/L	96	(31)

Persulfate (PS) assisted sonochemical degradation	Initial dye concentration: **5 mg/L**, initial PS concentration: 9 mg/L, temperature: 25 ºC, pH: 6, frequency: 585 kHz	95	(32)
Removal using enzyme (HRP)	Initial dye concentration: **370 mg/L**, H_2O_2 concentration: 0.3 mmol/L, enzyme concentration: 5.88 U/mL, temperature: **70 ºC**	94.7	(33)
Photo-catalytic degradation	Initial dye concentration: **20 mg/L**, catalyst concentration: 1 g/L, 500 W xenon lamp	94.3	(34)
Sonochemical removal	Initial dye concentration: **5 mg/L**, temperature: 25 ºC, pH=6, frequency: 585 kHz	94	(35)
Photo-catalytic degradation	Initial dye concentration: **10 mg/L**, P25@Pd/C catalyst concentration: 0.1 g/L, time: 120 min, 150 W Tungsten lamp, temperature: 25 ºC	91	(36)
Solar photo-catalytic degradation	Initial dye concentration: **123 mg/L**, AgBr–ZnO catalyst concentration: 2 g/L, pH=11, flow rate of air: 8.1 mL/s	50.8	(37)

Reaction Kinetics

In order to elucidate the kinetics of degradation of NBB with (Fe-Zn NPs)/C, kinetic data were obtained under optimum conditions (initial pH: 3.0, temperature: 40 °C, catalyst concentration: 0.25 g/ L) and then, the reaction rate expression was determined by performing mathematical analysis with the initial rate method.

Firstly, a reaction rate expression was suggested as shown in the following equation (Eq. 2):

$$-dC/(X_0.dt) = -dC^*/dt = k.C^n \quad \text{(Eq. 2)}$$

where C is the remaining dye concentration (mg/L), X_0 is the catalyst concentration (g/L), t is the reaction time (min), -dC*/dt is the degradation reaction rate for unit mass of catalyst (mg/(g_{cat}.min)), k is the degradation reaction rate constant, n is the order of degradation.

The linear form of Equation (2) according to the initial rate method was presented in Equation (3):

$$\ln(-dC^*/dt) = \ln k + n.\ln(C_0) \quad \text{(Eq. 3)}$$

In order to calculate the values of (-dC*/dt), the remaining dye concentrations ($C^*=C_t/X_0$) against the reaction time was plotted for the different initial dye concentrations (C_0). Then, the tangent lines were drawn at t=0 to the curves obtained for the different initial dye concentrations and the slopes of these tangent lines gave the values of (-dC*/dt).

After that, ln(-dC*/dt) vs ln(C_0) was plotted (given in Figure 10) and then, from the slope and intercept of the obtained linear line, the order of degradation (n) and the rate constant of the degradation (k) were calculated, respectively (38).

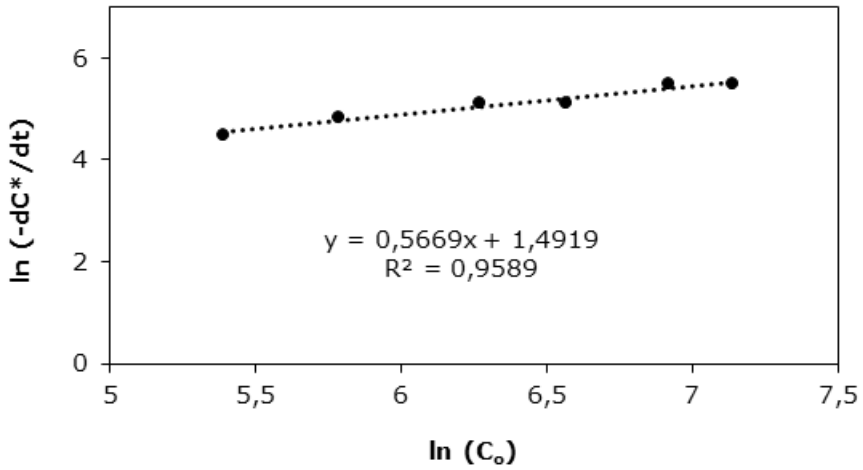

Figure 10. The plot of (-dC*/dt) vs ln(C_0) (initial pH: 3.0, temperature: 40 °C, catalyst concentration: 0.25 g/L).

The order of degradation (n) and rate constant of the degradation (k) were calculated as 0.5669 and 4.45, respectively. Accordingly, the reaction rate expression could be written as $-r_{degradation}$ (mg/(g_{cat}.min)) = $4.45(C)^{0.5669}$.

CONCLUSION

In this study, iron-zinc nanoparticles (Fe-Zn NPs) were firstly synthesized in the presence of glucose

by co-precipitation method using NaOH and then, the iron-zinc nanoparticles/carbon composite (Fe-Zn NPs)/C was synthesized by the hydrothermal carbonization of glucose in the solution containing Fe-Zn NPs. Next, the usability of [(Fe-ZnNPs)/C] as a heterogeneous catalyst in the removal of NBB dyestuff via Fenton-like reaction was investigated. Using the hydrochar as a supporter material for the nanoparticles provide not only lower the cost of the catalyst but also increase the catalytic activity by improving the catalyst properties. The removal could be achieved when both oxidant (H_2O_2) and catalyst (Fe-Zn NPs)/C were present together in the reaction medium, thus proving that the dyestuff was decolorized by Fenton-like reaction. The studies showed that the optimum initial pH, H_2O_2 concentration, temperature, and catalyst concentration for Fenton-like removal of NBB dyestuff with

[(Fe-ZnNPs)/C] were determined to be 3.0, 50 mM, and 0.25 g/L, respectively. The Fenton-like reaction order and rate constant were calculated as 0.5669 and 4.45, respectively. Moreover, this process enables to study at the wide initial pH and temperature range, which is an important advantage for the industrial applications. Consequently, the present study has revealed significant outputs to the synthesis of an effective Fenton-like heterogeneous catalyst, which could be important for the contribution to the related literature as well as the water treatment applications.

ACKNOWLEDGMENTS

This study was presented in 2nd Cilicia International Symposium on Engineering and Technology (CISET 2019) as an oral presentation and ievaluated by Journal of the Turkish Chemical Society Section B: Chemical Engineering.

REFERENCES

1. Kumar V, Ghime D, Ghosh P. Decolorization of textile dye Rifafix Red 3BN by natural hematite and a comparative study on different types of Fenton process. Chem Eng Commun [Internet]. 2019;0(0):1–10. Available from: https://doi.org/10.1080/00986445.2019.1652603

2. Tarkwa JB, Oturan N, Acayanka E, Laminsi S, Oturan MA. Photo-Fenton oxidation of Orange G azo dye: process optimization and mineralization mechanism. Environ Chem Lett [Internet]. 2019;17(1):473–9. Available from: https://doi.org/10.1007/s10311-018-0773-0

3. Katheresan V, Kansedo J, Lau SY. Efficiency of various recent wastewater dye removal methods: A review. J Environ Chem Eng. 2018;6(4):4676–97.

4. Khan J, Tariq M, Muhammad M, Mehmood MH, Ullah I, Raziq A, Akbar F, Saqib M, Rahim A, Niaz A. Kinetic and thermodynamic study of oxidative degradation of acid yellow 17 dye by fenton-like process: effect of HCO3−, CO32−,Cl− and SO42− on dye degradation. Bull. Chem. Soc. Ethiop. 2019;33(2):243–54.

5. Gu T, Dong H, Lu T, Han L, Zhan Y. Fluoride ion accelerating degradation of organic pollutants by Cu(II)-catalyzed Fenton-like reaction at wide pH range. J Hazard Mater [Internet]. 2019;377(January):365–70. Available from: https://doi.org/10.1016/j.jhazmat.2019.05.073

6. Vu AT, Xuan TN, Lee CH. Preparation of mesoporous Fe2O3·SiO2 composite from rice husk as an efficient heterogeneous Fenton-like catalyst for degradation of organic dyes. J Water Process Eng [Internet]. 2019;28(January):169–80. Available from: https://doi.org/10.1016/j.jwpe.2019.01.019

7. Yavari S, Mahmodi NM, Teymouri P, Shahmoradi B, Maleki A. Cobalt ferrite nanoparticles: Preparation, characterization and anionic dye removal capability. J Taiwan Inst Chem Eng [Internet]. 2016;59:320–9. Available from: http://dx.doi.org/10.1016/j.jtice.2015.08.011

8. Ma Q, Cui L, Zhou S, Li Y, Shi W, Ai S. Iron nanoparticles in situ encapsulated in lignin-derived hydrochar as an effective catalyst for phenol removal. Environ Sci Pollut Res. 2018;25(21):20833–40.

9. Gai C, Zhu N, Hoekman SK, Liu Z, Jiao W, Peng N. Highly dispersed nickel nanoparticles supported on hydrochar for hydrogen-rich syngas production from catalytic reforming of biomass. Energy Convers Manag [Internet]. 2019;183(January):474–84. Available from: https://doi.org/10.1016/j.enconman.2018.12.121

10. Wang T, Zhai Y, Zhu Y, Li C, Zeng G. A review of the hydrothermal carbonization of biomass waste for hydrochar formation: Process conditions, fundamentals, and physicochemical properties. Renew Sustain Energy Rev [Internet]. 2018;90(December 2016):223–47. Available from: https://doi.org/10.1016/j.rser.2018.03.071

11. Basso D, Castello D, Baratieri M, Fiori L. Hydrothermal carbonization of waste biomass: progress report and prospects. 21st Eur Biomass Conf Exhib. 2013;(June):1478–87.

12. Liang C, Liu Y, Li K, Wen J, Xing S, Ma Z, Heterogeneous photo-Fenton degradation of organic pollutants with amorphous Fe-Zn-oxide/hydrochar under visible light irradiation. Sep Purif Technol [Internet]. 2017;188:105–11. Available from: http://dx.doi.org/10.1016/j.seppur.2017.07.027

13. Kang SM, Li XL, Fan J, Chang J, Characterization of Hydrochars Produced by Hydrothermal Carbonization of Lignin, Cellulose, D-Xylose, and Wood Meal. Ind Eng Chem Res [Internet]. 2012;51:9023–9031. Available from: http://dx.doi.org/10.1021/ie300565d

14. Chen XY, Chen C, Zhang ZJ, Xie DH, Liu JW, Nitrogen/manganese oxides doped porous carbons derived from sodium butyl naphthalene sulfonate. J Colloid Interf Sci [Internet]. 2013;398:176–184. Available from: http://dx.doi.org/10.1016/j.jcis.2013.01.068

15. Khataee A, Kayan B, Kalderis D, Karimi A, Akay S, Konsolakis M. Ultrasound-assisted removal of Acid Red 17 using nanosized Fe3O4-loaded coffee waste hydrochar. Ultrason Sonochem [Internet]. 2017;35:72–80. Available from: http://dx.doi.org/10.1016/j.ultsonch.2016.09.004

16. Liu Z, Zhang F, Hoekman SK, Liu T, Gai C, Peng N. Homogeneously Dispersed Zerovalent Iron Nanoparticles Supported on Hydrochar-Derived Porous Carbon: Simple, in Situ Synthesis and Use for Dechlorination of PCBs. ACS Sustain Chem Eng. 2016;4(6):3261–7.

17. Gai C, Zhang F, Lang Q, Liu T, Peng N, Liu Z. Facile one-pot synthesis of iron nanoparticles immobilized into the porous hydrochar for catalytic decomposition of phenol. Appl Catal B Environ [Internet]. 2017;204:566–76. Available from: http://dx.doi.org/10.1016/j.apcatb.2016.12.005

18. Uzunoğlu D, Gürel N, Özkaya N, Özer A. The single batch biosorption of copper (II) ions on Sargassum acinarum. Desalin Water Treat [Internet]. 2014;52(7-9), 1514-1523. Available from: https://doi.org/10.1080/19443994.2013.789403

19. Khataee A, Kayan B, Kalderis D, Karimi A, Akay S, Konsolakis M. Ultrasound-assisted removal of Acid Red 17 using nanosized Fe3O4-loaded coffee waste hydrochar. Ultrason Sonochem [Internet] 2017;35, 72-80. Available from: https://doi.org/10.1016/j.ultsonch.2016.09.004

20. Çatlıoğlu FN, Akay S, Gözmen B, Turunc E, Anastopoulos I, Kayan B, Kalderis D. Fe-modified hydrochar from orange peel as adsorbent of food colorant Brilliant Black: process optimization and kinetic studies. Int J Environ Sci Tec [Internet]. 2020;17:1975–1990. Available from: https://doi.org/10.1007/s13762-019-02593-z

21. Ning Q, Liu Y, Liu S, Jiang L, Zeng G, Zeng Z, Kare Z. Fabrication of hydrochar functionalized Fe–Mn binary oxide nanocomposites: characterization and 17β-estradiol removal. Rsc Advances [Internet]. 2017;7(59), 37122-37129. Available from: https://doi.org/10.1039/c7ra06065c

22. Liu Z, Zhang F, Hoekman SK, Liu T, Gai C, Peng N. Homogeneously dispersed zerovalent iron nanoparticles supported on hydrochar-derived porous carbon: simple, in situ synthesis and use for dechlorination of PCBs. ACS Sustain Chem Eng [Internet]. 2016;4(6), 3261-3267. Available from: https://doi.org/10.1021/acssuschemeng.6b00306

23. Gai C, Yang T, Liu H, Liu Z, Jiao W. Hydrochar-Supported Bimetallic Ni–Cu Nanocatalysts for Sustainable H2 Production. ACS Appl. Nano Mater [Internet]. 2019;2(11), 7279-7289. Available from: https://doi.org/10.1021/acsanm.9b01762

24. Gai C, Zhang F, Lang Q, Liu T, Peng N, Liu Z. Facile one-pot synthesis of iron nanoparticles immobilized into the porous hydrochar for catalytic decomposition of phenol. Appl Catal B [Internet]. 2017;204, 566-576. Available from: http://dx.doi.org/10.1016/j.apcatb.2016.12.005

25. Hassani A, Çelikdağ G, Eghbali P, Sevim M, Karaca S, Metin Ö. Heterogeneous sono-Fenton-like process using magnetic cobalt ferrite-reduced graphene oxide (CoFe2O4-rGO) nanocomposite for the removal of organic dyes from aqueous solution. Ultrason Sonochem. 2018;40(August 2017):841–52.

26. Wang N, Zheng T, Zhang G, Wang P. A review on Fenton-like processes for organic wastewater treatment. J Environ Chem Eng [Internet]. 2016;4(1):762–87. Available from: http://dx.doi.org/10.1016/j.jece.2015.12.016

27. Ahmed SA, Soliman EM. Silica coated magnetic particles using microwave synthesis for removal of dyes from natural water samples: Synthesis, characterization, equilibrium, isotherm and kinetics studies. Appl Surf Sci [Internet]. 2013;284:23–32. Available from: http://dx.doi.org/10.1016/j.apsusc.2013.06.129

28. Ferkous H, Merouani S, Hamdaoui O. Sonolytic degradation of naphthol blue black at 1700kHz: Effects of salts, complex matrices and persulfate. J Water Process Eng [Internet]. 2016;9:67–77. Available from: http://dx.doi.org/10.1016/j.jwpe.2015.11.003

29. Ferkous H, Merouani S, Hamdaoui O, Rezgui Y, Guemini M. Comprehensive experimental and numerical investigations of the effect of frequency and acoustic intensity on the sonolytic degradation of naphthol blue black in water. Ultrason Sonochem [Internet]. 2015;26:30–9. Available from: http://dx.doi.org/10.1016/j.ultsonch.2015.02.004

30. Debnath S, Ballav N, Nyoni H, Maity A, Pillay K. Optimization and mechanism elucidation of the catalytic photo-degradation of the dyes Eosin Yellow (EY) and Naphthol blue black (NBB) by a polyaniline-coated titanium dioxide nanocomposite. Appl Catal B Environ [Internet]. 2015;163:330–42. Available from: http://dx.doi.org/10.1016/j.apcatb.2014.08.011

31. Reddy DR, Dinesh GK, Anandan S, Sivasankar T. Sonophotocatalytic treatment of Naphthol Blue Black dye and real textile wastewater using synthesized Fe doped TiO2. Chem Eng Process Process Intensif. 2016;99:10–8.

32. Ferkous H, Merouani S, Hamdaoui O, Pétrier C. Persulfate-enhanced sonochemical degradation of naphthol blue black in water: Evidence of sulfate radical formation. Ultrason Sonochem [Internet]. 2017;34:580–7. Available from: http://dx.doi.org/10.1016/j.ultsonch.2016.06.027

33. Onder S, Celebi M, Altikatoglu M, Hatipoglu A, Kuzu H. Decolorization of naphthol blue black using the horseradish peroxidase. Appl Biochem Biotechnol. 2011;163(3):433–43.

34. Mamba G, Mbianda XY, Mishra AK. Photocatalytic degradation of the diazo dye naphthol blue black in water using MWCNT/Gd,N,S-TiO2 nanocomposites under simulated solar light. Environ Sci (China) [Internet]. 2015;33:219–28. Available from: http://dx.doi.org/10.1016/j.jes.2014.06.052

35. Ferkous H, Hamdaoui O, Merouani S. Sonochemical degradation of naphthol blue black in water: Effect of operating parameters. Ultrason Sonochem [Internet]. 2015;26:40–7. Available from: http://dx.doi.org/10.1016/j.ultsonch.2015.03.013

36. Krishnakumar B, Kumar S, Gil JM, Pandiyan V, Aguiar A, Sobral AJFN. Highly active P25@Pd/C nanocomposite for the degradation of Naphthol Blue Black with visible light. J Mol Struct. 2018;1153:346–52.

37. Krishnakumar B, Swaminathan M. Solar photocatalytic degradation of Naphthol Blue Black. Desalin Water Treat. 2013;51(34–36):6572–9.

38. Fogler, H. Scott. Elements Of Chemical Reaction Engineering. Upper Saddle River, N.J. Prentice Hall International Editions, 3rd Edition, Page: 231.

JOTCS B
Journal of the Turkish Chemical Society
Section: B
Chemical Engineering
TURKISH CHEMICAL SOCIETY

Energy and Exergy Analysis on Bubbling Fluidized Bed Gasifier Using Aspen Plus Simulation

Senem Sezer[1], Uğur Özveren[1]*

[1]Marmara University, Faculty of Engineering, Department of Chemical Engineering, 34722, Istanbul, Turkey.

Abstract: In this study, exergy and energy analysis were investigated for gasification of almond shell in bubbling fluidized bed gasifier by using Aspen Plus simulation. The effect of temperature and steam/fuel ratio, which are important parameters for the gasification process, on energy and physical exergy values of syngas were examined. The results of the simulation showed that the exergy and energy values of the syngas were significantly affected by the change in gasifier temperature and steam/fuel ratio. Increasing the steam/fuel ratio influenced the energy and exergy value in a negative manner. However, H_2 and CO compositions in the syngas and energy and exergy values of the syngas increased with the enhancement of temperature. The developed bubbling fluidized bed gasifier model will create knowledge for researchers interested in the gasifier process.

Keywords: Gasification, bubbling fluidized bed gasifier, energy and exergy analysis, Aspen Plus, biomass.

Submitted: December 16, 2019. **Accepted:** November 13, 2020.

Cite this: Sezer S, Özveren U. Energy and Exergy Analysis on Bubbling Fluidized Bed Gasifier Using Aspen Plus Simulation. JOTCSB. 2020;3(2):55–64.

***Corresponding author.** E-mail: ugur.ozveren@marmara.edu.tr.

INTRODUCTION

Due to global concerns, researchers have focused to develop new and more efficient energy systems in order to supply the increasing energy demands in a sustainable way (1). Among renewable energy sources, biomass is getting considerable attention because of its low environmental impact, reducing carbon emissions, and the handle of converting organic-based wastes to useful energy (2). Biomass resources can be found in different forms such as forest residues, agricultural residues and crops, and municipal wastes. Biomass properties such as heating value, elemental composition, moisture, ash content, and volatile matter content are used to select proper biomass type for certain applications (3).

Biomass gasification is a promising process that converts biomass into synthesis gas (syngas) under different atmospheres such as O_2, CO_2, air and/or steam. Generally, the syngas can be used for generation of fuels, chemicals, and power, it produced in the gasification process is a combination of carbon monoxide (CO), methane (CH_4), carbon dioxide (CO_2) and hydrogen (H_2). Compared with air gasification, steam gasification obtains a better performance owing to more combustible gases are produced (4, 5). The gasification process takes place in the gasifier which is divided into three main groups with respect to their working principles, namely fixed bed, fluidized bed, and entrained flow gasifiers (6). They are selected according to operational conditions, fuel amounts, fuel properties such as shape, size, ash and moisture content (7). Bubbling bed gasifier is the type of fluidized bed, it has excellent heat and mass transfer, higher working capacity, and flexibility for the particle size of fuel (8).

Energy is conserved with respect to the first law of thermodynamics; it flows in or out of a system with heat transfers, mass flows, and work interactions. Exergy is the useful work potential of a certain amount of energy at specified state. Exergy measures and compares the ability to do work between energies of the same form. Energy consumption and losses of the system are evaluated by using the first law of thermodynamics. Exergy analysis is related to the second law of

thermodynamics that also provides information about the system's internal inefficiency (9-12). The destroyed exergy is related to the generated entropy. Exergy analysis can provide to design thermal system more efficient by decreasing the present inefficiencies.

Aspen Plus is a reliable software for designing and optimization of thermochemical processes. Researchers try to improve the gasification process for different operational conditions using by Aspen plus simulator based on the Gibbs free energy minimization. Biomass gasification technique is complex, and the process performance can be influenced by several parameters (13). Modeling and simulation can help to understand and analyze the effects of different parameters on the outcome variables (14, 15). Researchers have used Aspen Plus to model the gasification process. Beheshti et al.(16) modeled a bubbling fluidized bed gasifier under the steam-air atmosphere to evaluate effect of operational parameters on the syngas composition and hydrogen yield by using Aspen Plus. Begum et al. (17) examined the performance of the fixed bed gasifier model while the air-fuel ratio, gasifier temperature changed for different biomass feedstocks under steady-state condition via Aspen Plus simulation. Acar et al. (18) recently discussed the almond shell gasification process which used chemical equilibrium and restricted chemical equilibrium models. They compared the two models with experimental results and investigated the influence of gasification conditions on the syngas composition and lower heating value of syngas.

In this study, a new developed bubbling bed gasifier model was used to conduct almond shell gasification process under steam atmosphere by using Aspen Plus program. Unlike other literature studies, the main objective is to investigate the effect of temperature and steam/biomass ratio on the H_2 and CO composition of syngas accordingly exergy value. Performance of the gasification process of almond shell was evaluated where exergy issue is considered, and optimum operational conditions were determined for new developed bubbling bed gasifier model using Aspen Plus software.

MATERIALS AND METHODS

The determination of the biomass properties such as proximate, ultimate analysis and heating value is important to achieve efficient gasification performance. Almond shell is agricultural waste and has high energy potential to be used as feedstock in the bubbling fluidized bed gasifier (19). Ultimate and proximate analysis results of the almond shell, wood pellet, and tire have been used as feedstock in the developed model and validation respectively are presented in Table 1.

Table 1. Proximate and ultimate analysis of almond shell (20), wood pellet(21) and tire(22).

		Almond Shell	Wood Pellet	Tire
Proximate Analysis (wt %)	Volatile Matter	76.1	80.6	64.21
	Ash	3.04	0.89	6.68
	Moisture	7.85	9.8	0.68
	Fixed Carbon	20.86	18.51	29.11
Elemental Analysis (wt%)	Sulfur	0.03	0.004	2.48
	Oxygen	40.1	41.36	2.62
	Hydrogen	5.98	7.09	7.97
	Carbon	50.14	50.57	80.1
	Nitrogen	0.74	0.089	0.15

A bubbling fluidized bed gasifier model for the steam gasification of almond shell was conducted in the Aspen Plus process simulator through the combination of reactors, mixers, heat exchangers, and separators. Stream and block information were specified, and the thermodynamic property method was selected as Soave-Redlich-Kwong to perform the simulation, where HCOALGEN and the DCOALIGT models as a physical property method was selected to calculate the enthalpy and density of almond shell. Steam was selected as a gasifying agent. The bubbling fluidized bed gasifier model is shown in Figure 1.

Gibbs's free energy minimization was implemented in the developed model. Bubbling fluidized bed gasifier was modeled under some assumptions:

- The model is in a steady-state, gasification parameters do not change with time.
- All gases are ideal.
- There is no pressure decrease in the gasifier.

- The ash in the almond shell is inert and does not participate in the gasification reactions.
- The temperature distribution is uniform in the gasifier.
- All the reactions reach equilibrium.

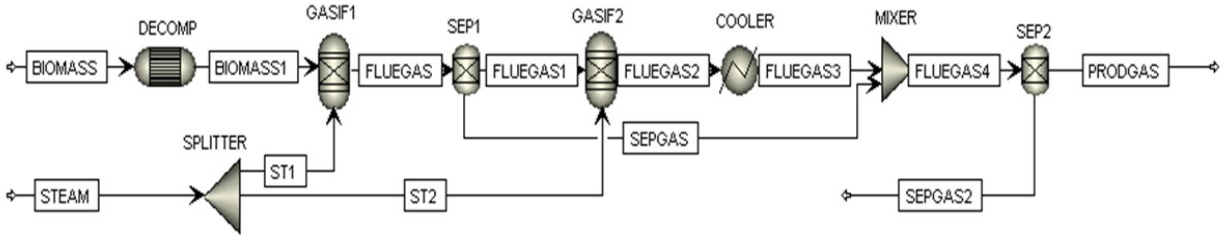

Figure 1: Bubbling fluidized bed gasifier flowsheet in Aspen Plus.

Almond shell was introduced with its proximate and ultimate analysis results as nonconventional component to the stream named BIOMASS temperature at 20 °C with 25 kg/h flow rate. In DECOMP reactor, RYIELD type reactor was selected and the feed was decomposed into its conventional components based on the sulfur, proximate, and ultimate analyses of the almond shell. RGIBBS reactor was used to represent pyrolysis and gasification zones. Low and high temperature pyrolysis takes place in the GASIF1 the temperature around 300 °C. SEP1 block separates the certain amount of CH_4 and CO before the gasification part. Gasification reactions are formed in GASIF2 reactor and operation temperature changes between 700-1000 °C. Steam flow rate is changed between 10-40 kg/h and flow is split into two streams equally to create a steam atmosphere in the GASIF1 and GASIF2 by using SPLITTER. COOLER is used to cool or keep constant the syngas temperature at 800 °C after GASIF2 reactor. SEPGAS and FLUGAS3 is mixed in the MIXER. Water, ash, and H_2S were separated from FLUEGAS4 to clean product gas via SEP2 block. Gasification reactions which take place in bubbling bed gasifier are submitted in Table 2 (23).

Gasification agent, biomass properties, and operating conditions affect the gasification reactions directly.

Table 2. Gasification reactions in bubbling fluidized bed gasifier

$C+2H_2 \leftrightarrow CH_4$ (methane formation reaction)	(1)
$C + 1/2O_2 \rightarrow CO$ (partial oxidation reaction)	(2)
$CO + H_2O \leftrightarrow CO_2 + H_2$ (water gas shift reaction)	(3)
$C + CO_2 \leftrightarrow 2CO$ (Boudouard reaction)	(4)
$H_2 + S \rightarrow H_2S$	(5)
$C + H_2O \leftrightarrow CO + H_2$ (water gas reaction)	(6)
$CH_4 + H_2O \leftrightarrow CO + 3H_2$ (steam reforming reaction)	(7)
$C + O_2 \rightarrow CO_2$ (complete oxidation reaction)	(8)
$H_2 + 0.5O_2 \rightarrow H_2O$ (hydrogen oxidation)	(9)

The model in this study was simulated between the gasifier temperature 700-1000 °C, and the steam flow rate 10-40 kg/h to investigate the effect of operational conditions on the syngas composition and exergy value. Sensitivity analysis was implemented to conduct parametric studies.

RESULTS

Model Validation

The developed model was successfully validated with two data sets from literature. In the first data (21), the wood pellet was used as a feedstock and gasification process carried out at 800 °C under air atmosphere. The model was also validated with steam gasification data (22), where tire samples were used as fuel under steam atmosphere in bubbling fluidized bed gasifier. The syngas composition of the model is approximate to experimental gas composition as shown in Table 3.

The model validation results from literature as seen on Table 3 show that the model is robust and have worked properly. However, CH_4 compositions are quite different from experimental results in the literature, while H_2, CO, and CO_2 compositions are very close. Because the model works thermodynamic equilibrium based and residence time could be different in the Aspen Plus model and experimental study.

Parametric Study

Sensitivity analysis was applied to conduct parametric studies after model validation. The effect of gasifier temperature and steam/biomass ratio on the syngas composition and exergy value have been examined.

Table 3. Model validation results with air (21) and steam (22) gasification data sets.

Model validation result with air (21) experimental data set		
Wood Pellet	Fuel (kg/h)	34
Gasifier - 800°C	Air (Nm^3/h)	37
Gas Composition	**Literature (%)**	**Model (%)**
H_2	14.5	15.67
CO_2	16	16.44
CO	13.8	13.91
CH_4	4	9.09
Model validation result with steam(22) experimental data set		
Tire Sample	Fuel (kg/h)	0.876
Gasifier – 770°C	Steam (kg/h)	0.331
Gas Composition	**Literature (%)**	**Model (%)**
H_2	48.81	47.87
CO_2	3.30	3.56
CO	3.89	3.2
CH_4	26.37	14.3

Effect of Temperature on Syngas Composition

Gasifier temperature affects the syngas composition as seen in Figure 2. Because of endothermic reactions occurring in the gasifier, syngas composition changes with increasing temperature.

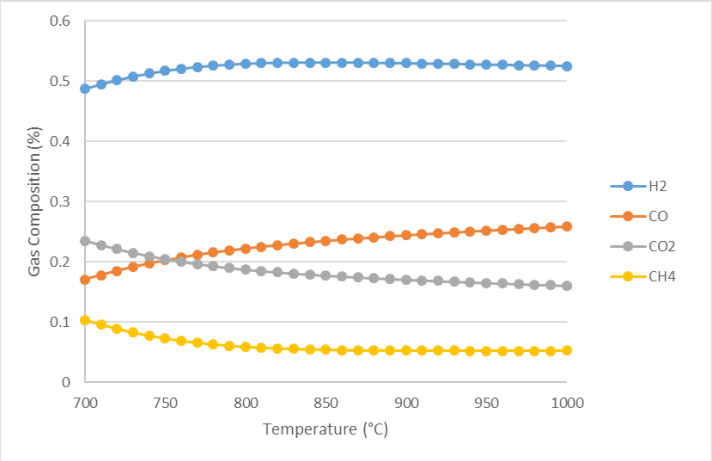

Figure 2. Effect of temperature on the syngas composition.

H_2 and CO composition increased with increasing temperature. On the other hand, CH_4 and CO_2 compositions showed an opposite tendency versus gasifier temperature. This is because higher temperature favors the steam and methane reforming reactions. Boudouard reaction also promotes CO formation, while the CO_2 concentration decreased with enhancing the temperature due to that is more effective when the temperature is higher than 800 °C. H_2 composition reached the maximum value at 850 °C. Increasing temperature above 850°C affected the H_2 concentration negatively. Former studies in the literature show the similar results for effect of temperature on the syngas composition (24-26).

Effect of Temperature on Exergy Value of Syngas

Exergy value is utilized to evaluate system performance. Figure 3 shows the change of syngas exergy value with the temperature in the bubbling fluidized bed gasifier. The studies about the syngas exergy value was discussed in the literature and our results show consistency with them (27, 28).

Exergy value of the syngas is the total value of chemical and physical exergies. Gasifier temperature is associated with physical and chemical exergies as increasing potential energy value and combustible components such as H_2 and CO in the syngas. H_2 concentration change showed the same trend with the exergy value of syngas. Both reached the maximum value at 850°C.

Sensitivity analysis results in Aspen Plus simulation for syngas exergy value according to temperature change were presented in Figure 4.

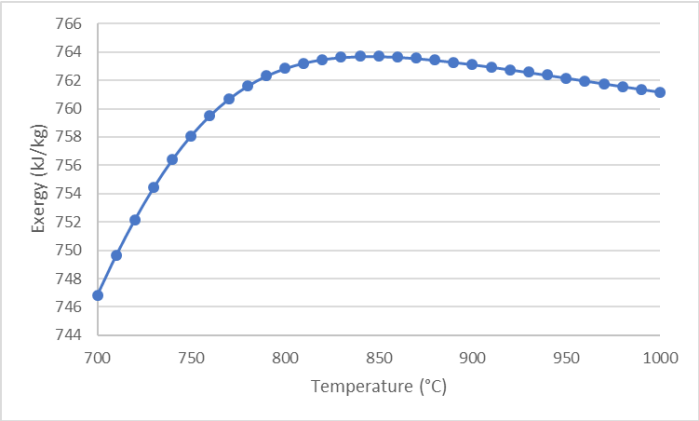

Figure 3. Effect of temperature on the syngas exergy value.

Effect of steam flow rate on the syngas composition
The steam flow rate is an important parameter for steam gasification. Enrichment of the steam flow rate affected the synthesis gas composition as shown in Figure 5. H_2 and CO_2 increased and CH_4 and CO decreased with increasing steam flow rate.

With the addition of steam, water-gas shift, water-gas, and steam methane reforming reactions shift to the product side according to Le Châtelier's principle (29). As a result of all reactions, H_2 concentration increased and CH_4 concentration decreased with steam increases. Increasing of steam flow rate is leading to more complete oxidation reaction, therefore, CO_2 concentration increases and CO concentration decreases. In this study, obtained results from Aspen Plus model show good agreement with the literature studies (30).

Effect of steam flow rate on the syngas exergy value

The effects of steam flow rate on the exergy of syngas were investigated. Figure 6 shows that syngas exergy value, from almond shell gasification under steam atmosphere, demonstrated an increasing trend with steam flow rate increases.

The trend in exergy increase from Figure 6 could be explained by encouragement of hydrogen formation as steam was supplied, which leads to higher exergy content at lower steam flow rate under 30 kg/h. The later increases in the exergy values were resulted from the decreases in the yields of CO. The results show that influence of steam flow rate on the syngas exergy value has similar behavior with literature studies (31).

The results are taken from Aspen Plus and presented in graphic 6 can be seen in the Figure 7 as screenshot in Aspen Plus simulation.

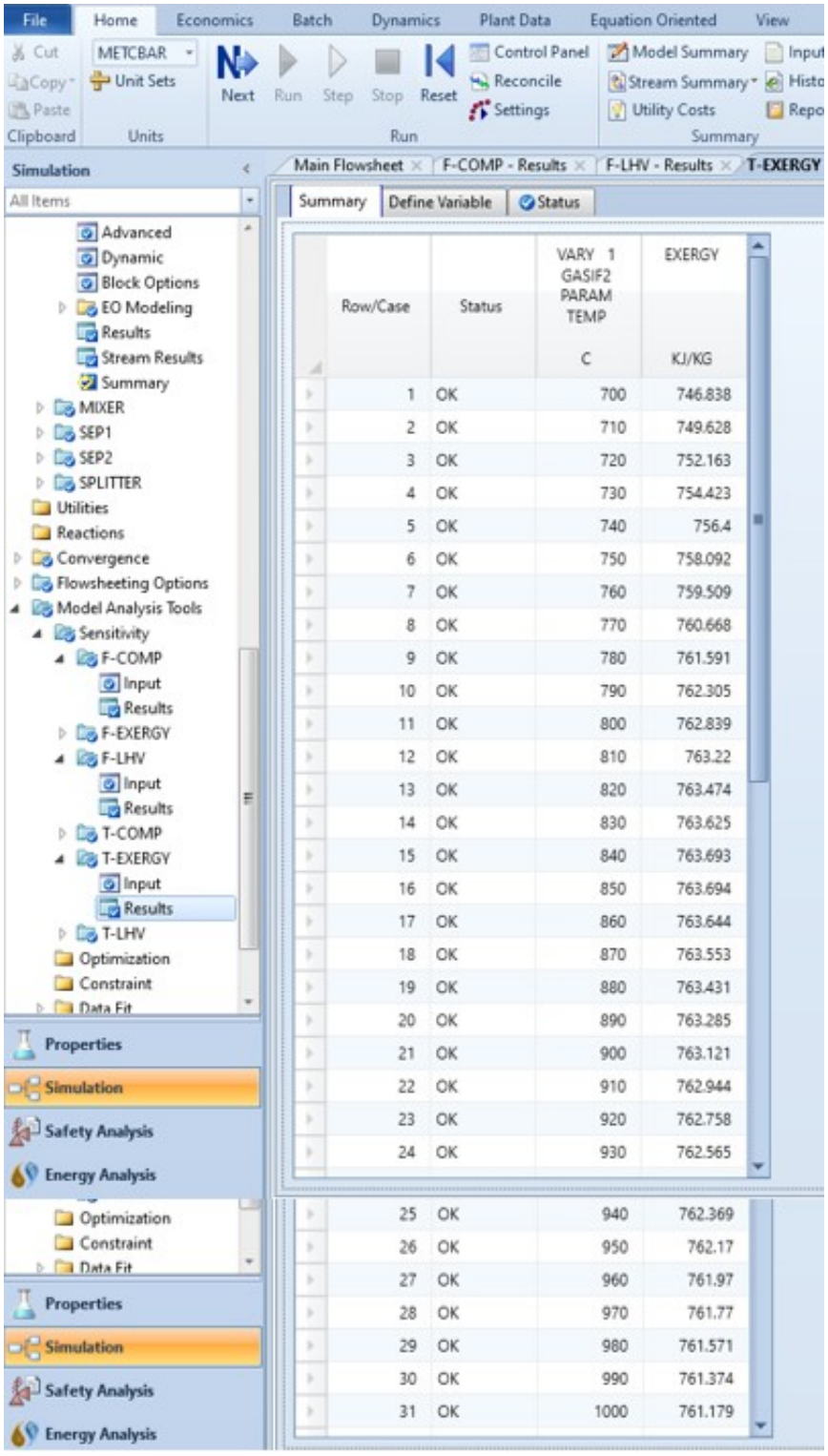

Figure 4. Sensitivity analysis results for effect of temperature on the syngas exergy value in Aspen Plus.

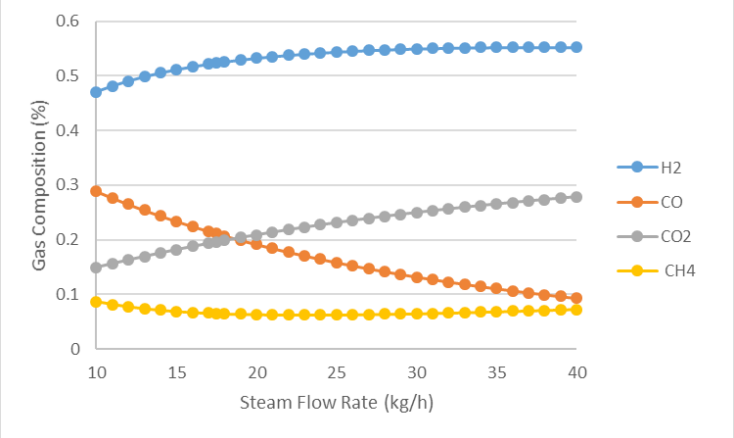

Figure 5. Effect of steam flow rate on the syngas composition.

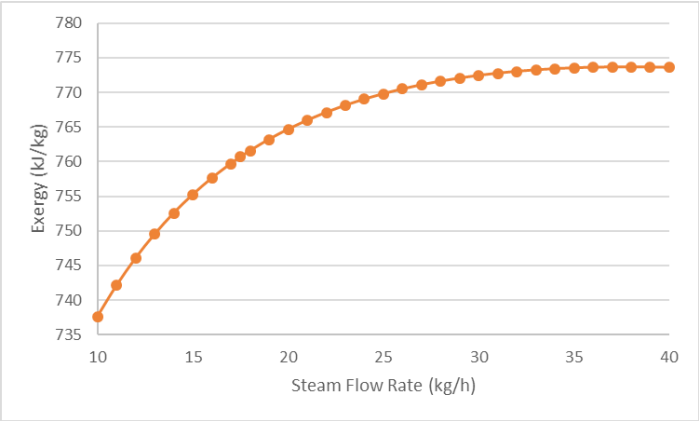

Figure 6. Effect of steam flow rate on the syngas exergy value.

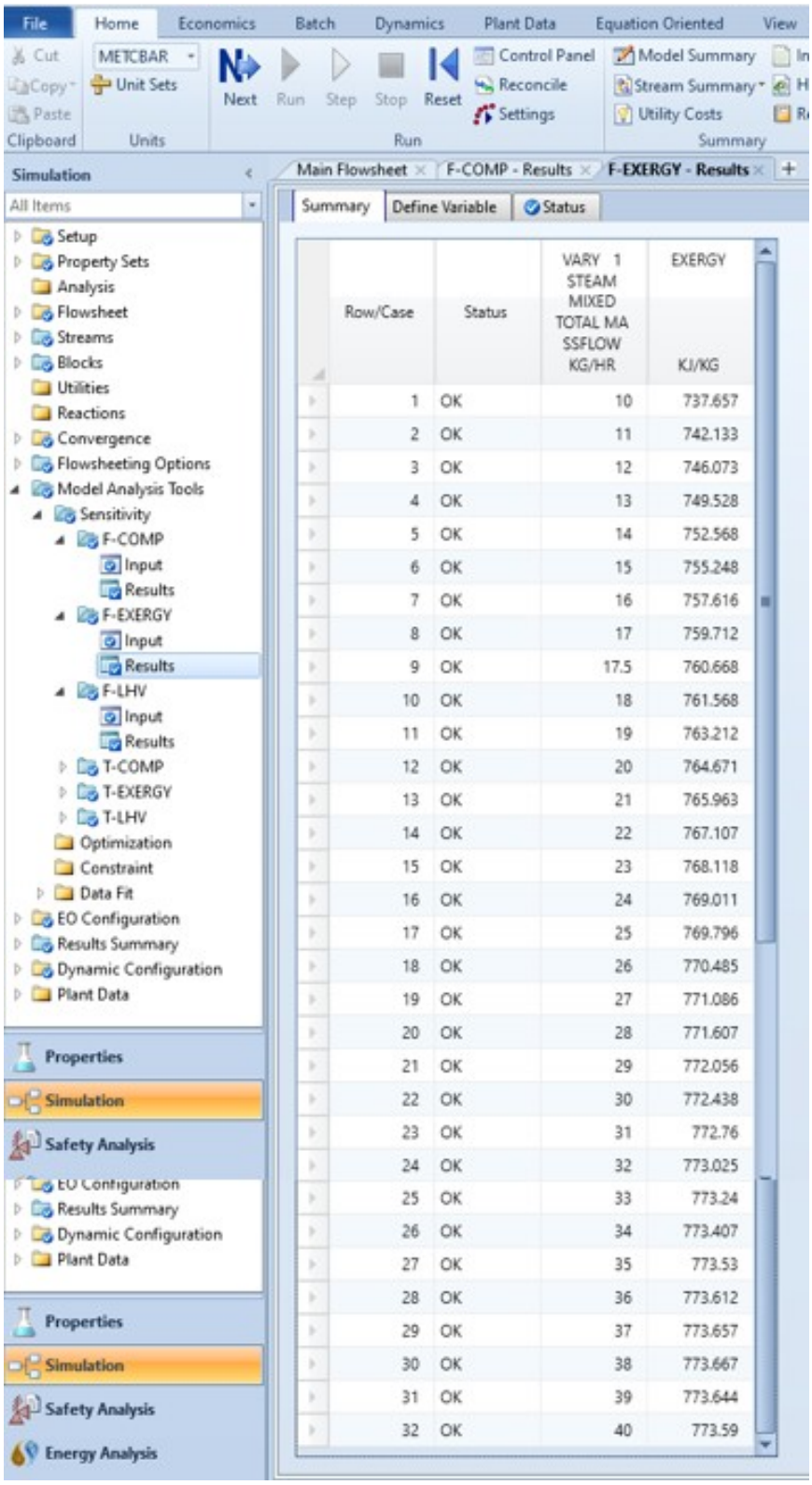

Figure 7. Sensitivity analysis results for effect of steam flow rate on the syngas exergy value in Aspen Plus.

CONCLUSION

The following conclusive remarks were drawn:

- The developed bubbling fluidized bed model was successfully validated with experimental data sets from literature.
- Changing the gasifier temperature showed a significant effect on the syngas composition. H_2 composition increased from 48.74% to 53.11% between the temperatures 700-850 °C, and reached the maximum value at 850 °C, while CO content in the syngas increased from 17.05% to 23.48%.

- Increasing the gasifier temperature enhanced the system energy potential, therefore, the exergy value of syngas increased from 746.83 to 763.70 kJ/kg between the temperature 700 and 850 °C.
- Results represented that the steam flow rate showed considerable effects on H_2 and CO composition in the syngas. H_2 content increased between %47 and %55 and CO content decreased from 28% to 9%, while the steam flow rate raised from 10 to 40 kg/h. Furthermore, the exergy value of syngas increased from 737 to 773 kJ/kg.

REFERENCES

1. Siddiqui O, Dincer I, Yilbas B. Development of a novel renewable energy system integrated with biomass gasification combined cycle for cleaner production purposes. Journal of Cleaner Production. 2019:118345.

2. Rodríguez-Monroy C, Mármol-Acitores G, Nilsson-Cifuentes G. Electricity generation in Chile using non-conventional renewable energy sources–A focus on biomass. Renewable and Sustainable Energy Reviews. 2018;81:937-45.

3. Moilanen A, Nasrullah M, Kurkela E. The effect of biomass feedstock type and process parameters on achieving the total carbon conversion in the large scale fluidized bed gasification of biomass. Environmental progress & sustainable energy. 2009;28(3):355-9.

4. Hosseini M, Dincer I, Rosen MA. Steam and air fed biomass gasification: comparisons based on energy and exergy. International journal of hydrogen energy. 2012;37(21):16446-52.

5. Udomsirichakorn J, Salam PA. Review of hydrogen-enriched gas production from steam gasification of biomass: the prospect of CaO-based chemical looping gasification. Renewable and sustainable energy reviews. 2014;30:565-79.

6. Sansaniwal S, Rosen M, Tyagi S. Global challenges in the sustainable development of biomass gasification: an overview. Renewable and Sustainable Energy Reviews. 2017;80:23-43.

7. Mazaheri N, Akbarzadeh A, Madadian E, Lefsrud M. Systematic review of research guidelines for numerical simulation of biomass gasification for bioenergy production. Energy conversion and management. 2019;183:671-88.

8. Bach Q-V, Gye H-R, Lee C-J. Process modeling for steam biomass gasification in a dual fluidized bed gasifier. Computer Aided Chemical Engineering. 44: Elsevier; 2018. p. 343-8.

9. Kwofie E, Ngadi M, Sotocinal S. Thermodynamic evaluation of a rice husk fired integrated steam and hot air generation unit for rice parboiling. Energy. 2017;128:39-49.

10. Kanoglu M, Işık SK, Abuşoğlu A. Performance characteristics of a diesel engine power plant. Energy Conversion and Management. 2005;46(11-12):1692-702.

11. Kanoglu M, Dincer I, Rosen MA. Understanding energy and exergy efficiencies for improved energy management in power plants. Energy Policy. 2007;35(7):3967-78.

12. Dincer I, Hussain M, Al-Zaharnah I. Analysis of sectoral energy and exergy use of Saudi Arabia. International Journal of Energy Research. 2004;28(3):205-43.

13. Nemtsov D, Zabaniotou A. Mathematical modelling and simulation approaches of agricultural residues air gasification in a bubbling fluidized bed reactor. Chemical Engineering Journal. 2008;143(1-3):10-31.

14. Gómez-Barea A, Leckner B. Modeling of biomass gasification in fluidized bed. Progress in Energy and Combustion Science. 2010;36(4):444-509.

15. Couto N, Rouboa A, Silva V, Monteiro E, Bouziane K. Influence of the biomass gasification processes on the final composition of syngas. Energy Procedia. 2013;36:596-606.

16. Beheshti S, Ghassemi H, Shahsavan-Markadeh R. Process simulation of biomass gasification in a bubbling fluidized bed reactor. Energy conversion and management. 2015;94:345-52.

17. Begum S, Rasul M, Akbar D, Ramzan N. Performance analysis of an integrated fixed bed gasifier model for different biomass feedstocks. Energies. 2013;6(12):6508-24.

18. Acar MC, Böke YE. Simulation of biomass gasification in a BFBG using chemical equilibrium model and restricted chemical equilibrium method. Biomass and Bioenergy. 2019;125:131-8.

19. Quesada L, Pérez A, Calero M, Blazquez G, Martín-Lara M. Reaction schemes for estimating kinetic parameters of thermal decomposition of native and metal-loaded almond shell. Process Safety and Environmental Protection. 2018;118:234-44.

20. NREL Transforming Energy [Available from: https://www.nrel.gov/rredc/biomass_resource.html.

21. Kim YD, Yang CW, Kim BJ, Kim KS, Lee JW, Moon JH, et al. Air-blown gasification of woody biomass in a bubbling fluidized bed gasifier. Applied energy. 2013;112:414-20.

22. Karatas H, Olgun H, Akgun F. Experimental results of gasification of waste tire with air&CO2, air&steam and steam in a bubbling fluidized bed gasifier. Fuel processing technology. 2012;102:166-74.

23. AlNouss A, McKay G, Al-Ansari T. A techno-economic-environmental study evaluating the potential of oxygen-steam biomass gasification for the generation of value-added products. Energy Conversion and Management. 2019;196:664-76.

24. Skoulou V, Zabaniotou A, Stavropoulos G, Sakelaropoulos G. Syngas production from olive tree cuttings and olive kernels in a downdraft fixed-bed gasifier. International journal of hydrogen energy. 2008;33(4):1185-94.

25. Begum S, Rasul MG, Akbar D, Ramzan N. Performance analysis of an integrated fixed bed gasifier model for different biomass feedstocks. Energies. 2013;6(12):6508-24.

26. Nikoo MB, Mahinpey N. Simulation of biomass gasification in fluidized bed reactor using ASPEN PLUS. Biomass and bioenergy. 2008;32(12):1245-54.

27. Lu Y, Jin H, Guo L, Zhang X, Cao C, Guo X. Hydrogen production by biomass gasification in supercritical water with a fluidized bed reactor. International Journal of Hydrogen Energy. 2008;33(21):6066-75.

28. Zhang Y, Li B, Li H, Liu H. Thermodynamic evaluation of biomass gasification with air in autothermal gasifiers. Thermochimica Acta. 2011;519(1-2):65-71.

29. Shehzad A, Bashir MJ, Sethupathi S. System analysis for synthesis gas (syngas) production in Pakistan from municipal solid waste gasification using a circulating fluidized bed gasifier. Renewable and Sustainable Energy Reviews. 2016;60:1302-11.

30. AlNouss A, Parthasarathy P, Shahbaz M, Al-Ansari T, Mackey H, McKay G. Techno-economic and sensitivity analysis of coconut coir pith-biomass gasification using ASPEN PLUS. Applied Energy. 2020;261:114350.

31. Samimi F, Marzoughi T, Rahimpour MR. Energy and exergy analysis and optimization of biomass gasification process for hydrogen production (based on air, steam and air/steam gasifying agents). International Journal of Hydrogen Energy. 2020.